ELEMENTA
Science of the Anthropocene

Itkin, P, et al. 2023. Sea ice and snow characteristics from year-long transects at the MOSAiC Central Observatory. *Elem Sci Anth*, 11: 1. DOI: https://doi.org/10.1525/elementa.2022.00048

RESEARCH ARTICLE

Sea ice and snow characteristics from year-long transects at the MOSAiC Central Observatory

Polona Itkin[1,2,*], Stefan Hendricks[3], Melinda Webster[4], Luisa von Albedyll[3], Stefanie Arndt[3], Dmitry Divine[5], Matthias Jaggi[6], Marc Oggier[7], Ian Raphael[8], Robert Ricker[9], Jan Rohde[3], Martin Schneebeli[6], and Glen E. Liston[2]

Repeated transects have become the backbone of spatially distributed ice and snow thickness measurements crucial for understanding of ice mass balance. Here we detail the transects at the Multidisciplinary drifting Observatory for the Study of Arctic Climate (MOSAiC) 2019–2020, which represent the first such measurements collected across an entire season. Compared with similar historical transects, the snow at MOSAiC was thin (mean depths of approximately 0.1–0.3 m), while the sea ice was relatively thick first-year ice (FYI) and second-year ice (SYI). SYI was of two distinct types: relatively thin level ice formed from surfaces with extensive melt pond cover, and relatively thick deformed ice. On level SYI, spatial signatures of refrozen melt ponds remained detectable in January. At the beginning of winter the thinnest ice also had the thinnest snow, with winter growth rates of thin ice (0.33 m month^{-1} for FYI, 0.24 m month^{-1} for previously ponded SYI) exceeding that of thick ice (0.2 m month^{-1}). By January, FYI already had a greater modal ice thickness (1.1 m) than previously ponded SYI (0.9 m). By February, modal thickness of all SYI and FYI became indistinguishable at about 1.4 m. The largest modal thicknesses were measured in May at 1.7 m. Transects included deformed ice, where largest volumes of snow accumulated by April. The remaining snow on level ice exhibited typical spatial heterogeneity in the form of snow dunes. Spatial correlation length scales for snow and sea ice ranged from 20 to 40 m or 60 to 90 m, depending on the sampling direction, which suggests that the known anisotropy of snow dunes also manifests in spatial patterns in sea ice thickness. The diverse snow and ice thickness data obtained from the MOSAiC transects represent an invaluable resource for model and remote sensing product development.

Keywords: Sea ice, Snow, Arctic

1. Introduction

The shrinking Arctic ice cover has been highlighted as one of the most detectable consequences of modern climate change. Summer and winter sea ice extents have been reduced by about 50% and 10%, respectively, over the past four decades (Onarheim et al., 2018; Stroeve and Notz, 2018). The sea ice lifespan has shortened such that multi-year ice (MYI) has become rare, and has largely been replaced by second-year ice (SYI) and first-year ice (FYI) (Kwok, 2018; Stroeve and Notz, 2018). Over a similar period, sea ice thickness has decreased by 65% (Lindsay and Schweiger, 2015), while sea ice drift has accelerated by 5% (Spreen et al., 2011), likely with an associated increase in deformation rates (Rampal et al., 2009; Itkin et al., 2017). While detailed observations of these trends are highly desirable, sea ice thickness estimates from satellite observations in particular are subject to significant uncertainties (Ricker et al., 2014; Zygmuntowska et al., 2014; Jutila et al., 2021).

These uncertainties are largely attributed to the fact that the sea ice, despite being very thin, has a complex structure that changes in time and is highly heterogeneous in space. Sea ice undergoes a strong seasonal cycle, from melting sea ice in summer to snow-covered winter ice that thickens due to freezing of the surface ocean and sea ice deformation. Snow on sea ice accumulates after sea ice freeze-up in fall and early winter. In its contrasting

[1] UiT–The Arctic University of Norway, Tromsø, Norway
[2] Cooperative Institute for Research in the Atmosphere, Colorado State University, Fort Collins, CO, USA
[3] Alfred Wegener Institute, Helmholtz Centre for Polar and Marine Research, Bremerhaven, Germany
[4] University of Alaska Fairbanks, Geophysical Institute, AK, USA
[5] Norwegian Polar Institute, Tromsø, Norway
[6] Swiss Federal Institute for Forest, Snow and Landscape Research (WSL), Institute for Snow and Avalanche Research (SLF), Davos, Switzerland
[7] International Arctic Research Center, University of Alaska Fairbanks, AK, USA
[8] Dartmouth College, Thayer School of Engineering, Hanover, NH, USA
[9] NORCE Norwegian Research Centre, Tromsø, Norway

* Corresponding author:
Email: polona.itkin@uit.no

roles as a potent insulator and one of the most optically reflective materials on the planet, snow is a strong regulator of sea ice growth and melt (Sturm and Massom, 2009; Webster et al., 2018). Summer sea ice is mostly snow-free (Warren et al., 1999), and much of the snow meltwater pools into puddles called melt ponds (Polashenski et al., 2012), which reduce the surface albedo and enhance ice melt (Perovich et al., 2011).

In addition, sea ice is brittle and deforms under the forcing of atmosphere and ocean, piling into pressure ridges and exposing the ocean surface as leads. Deformed sea ice that is thick and rough makes up about one third of all Arctic sea ice (Hansen et al., 2013; Kwok and Cunningham, 2016; Itkin et al., 2018; Koo et al., 2021). Large pressure ridges that are seemingly randomly spaced at distances of tens to hundreds of meters (Castellani et al., 2014; Itkin et al., 2018; Farrell et al., 2020) are a known aerodynamic snow barrier (Sturm et al., 2002a) that can catch up to 22% of all snow cover (Liston et al., 2018). The role of small deformation features like ice rubble (small ice blocks that are not part of pressure ridge sails) and hummocks (smoothed deformed ice transformed by summer melt) remains under-explored. Erosion and deposition of snow by wind causes spatio-temporal variability at a few-meter scale on level ice even in the absence of deformed ice (Iacozza and Barber, 1999; Sturm et al., 2002a; Liston et al., 2018). These snow dunes—repetitive undulations in snow topography—affect the heat fluxes between ocean and atmosphere (Sturm et al., 2002b), yet there is limited evidence of how such heterogeneous snow distribution affects local sea ice thickness variability or, in turn, how the surface roughness of the sea ice affects spatial heterogeneity of the snow cover.

The sea ice seasonal cycle and snow-ice interactions have likely gained importance with the transition of Arctic sea ice from perennial to seasonal, but observational data to quantify this transition are scarce. Snow depth and sea ice thickness transects have been conducted on most polar expeditions since the Surface Heat Budget of the Arctic Ocean (SHEBA) project in 1998 (Eicken et al., 2001; Haas et al., 2017; Rösel et al., 2018), but a year-long record of combined snow and sea ice transects has not been collected until now. From October 2019 to September 2020 the Multidisciplinary drifting Observatory for the Study of Arctic Climate (MOSAiC) team observed the full seasonal development of "new" Arctic sea ice (Shupe et al., 2020; Nicolaus et al., 2022). Several other remote sensing, airborne or indirect mass-balance measurements will utilize this transect data for validation and scaling. The complementary measurements of sea ice mass balance (by stakes, ice mass balance buoys), ice and snow structure, surface elevation, and a suite of state-of-the-art field observations from atmosphere, ocean, chemistry and ecosystem make the MOSAiC transect measurements especially valuable for understanding linkages within the Arctic climate system.

The aims of this paper are 1) to give a comprehensive description of the MOSAiC transect dataset; 2) to present the MOSAiC seasonal time series and compare it to previous datasets; and 3) to evaluate winter sea ice and snow interactions based on these data. To address these three aims, we constructed this article to include a sizeable section (Section 2) on the details of both sampling techniques and methods for data analysis methods. The results and discussion are merged into one section (Section 3) divided thematically into similarities between ice types (Section 3.1), seasonal time series (Section 3.2), and interaction between winter snow and ice (Section 3.3). Summary conclusions are given in Section 4.

2. Methods and data

At MOSAiC, transects were sampled over diverse ice types in three separate Central Observatories (CO) that drifted with the Transpolar Drift current as shown on **Figure 1**. The first CO was sampled between October 2019 and May 2020; the second CO, in June and July 2020; and the third CO, in August and September 2020. Details on the MOSAiC drift can be found in Shupe et al. (2020) and Nicolaus et al. (2022). The MOSAiC transect sampling is detailed in Section 2.3.

2.1. Historical methods leading to this study

The first Arctic seasonal snow depth data were collected on drifting stations at clusters of snow stakes (Untersteiner, 1961). On the former Soviet Union's drifting ice stations (1937–1991) the "snowlines," as the first snow transects were called, came into standard use after 1955 (Radionov et al., 1997; Warren et al., 1999). There, 50–100 snow depth measurements were taken along 500–1000 m long repeat transects with 10-day to monthly intervals. The measurements were made mainly on MYI. Warren et al. (1999) merged over 33,000 measurements from these snowlines spanning 1954–1991 into a monthly climatology of snow depth. An example of snow depth climatology for January is shown in **Figure 1**. For the climatological snow depths, interannual variability was estimated by standard deviation of anomalies from multi-year trends for each month. This variability is not spatially distributed as it is given as constant monthly values for the entire Arctic Ocean.

Similar to previous drifting ice stations, SHEBA (from October 1997 to October 1998) had continuous snow depth measurements taken at few-meter spacing along a 500-m "main snowline" across MYI that also included hummocks (Sturm et al., 2002a). A lead that occurred in January cut through the line, temporarily truncated the line and afterwards caused a decrease in the observed snow depth as low values over the refrozen lead were included (Sturm et al., 2002a). FYI snowline sampling was also attempted at SHEBA, but it was soon destroyed by ice deformation. The SHEBA drift track in the central Arctic is shown on **Figure 1**.

Repeated point data on sea ice thickness have been collected traditionally using "hot wires." Metal wires deployed through the ice are heated and loosened from the ice by electric currents, allowing the user to pull the gauge up and measure changes in ice thickness (Untersteiner, 1961; Perovich et al., 2003). Such installations are limited in their spatial and temporal resolution due to the manual nature of the measurement. No equivalents to the

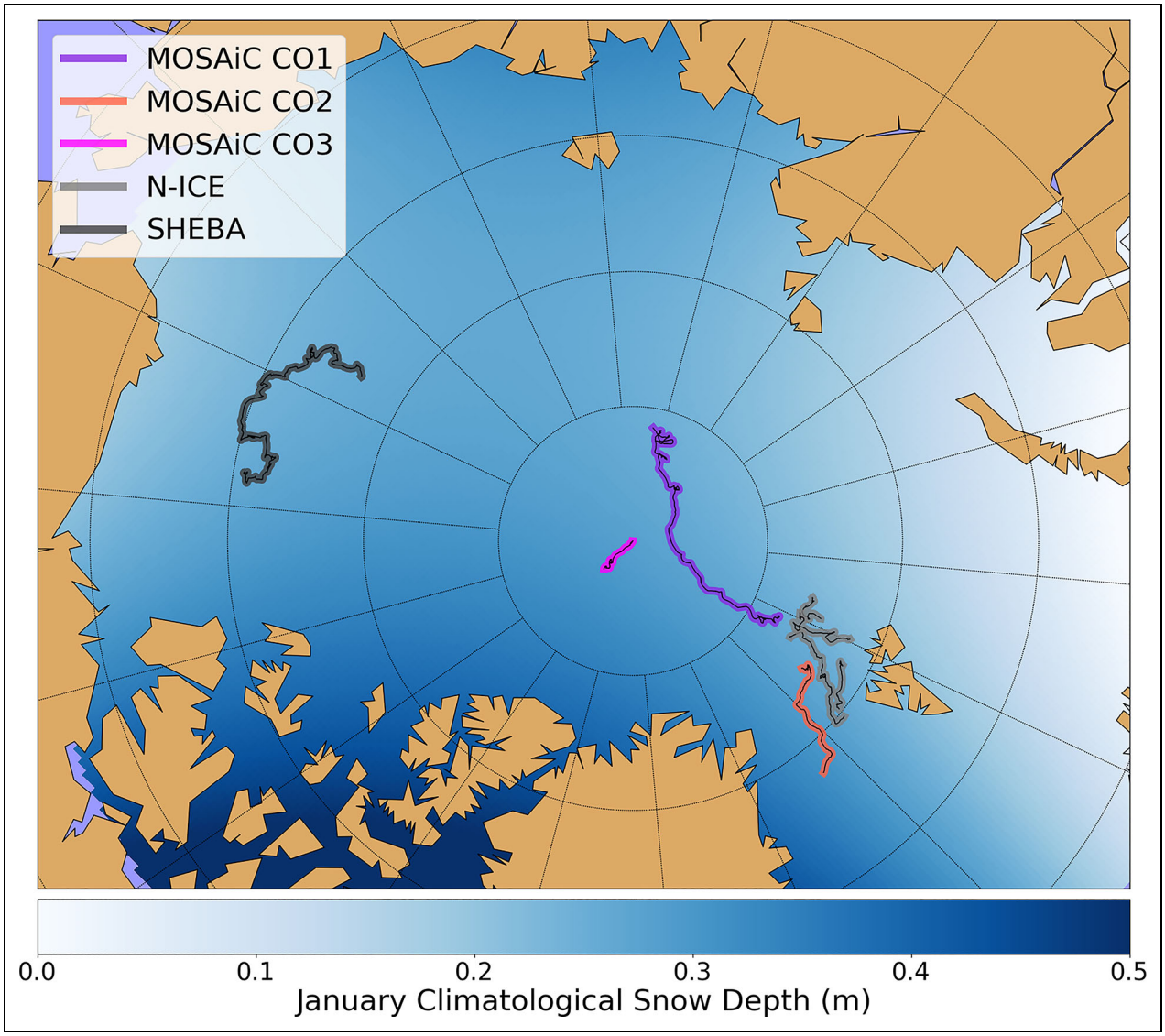

Figure 1. Drift tracks of all three MOSAiC Central Observatories (CO), N-ICE 2015 and SHEBA 1997/98. The first CO (CO1) operated from October 2019 to May 2020. The second (CO2) and third CO (CO3) operated in June and July, and August and September 2020, respectively. Map background color is snow depth from the Warren Climatology (Warren et al., 1999).

former Soviet Union snowlines existed until the development of electromagnetic induction (EM) methods (Eicken et al., 2001). Both Magnaprobe and EM devices (described further in Sections 2.2.1 and 2.2.2) enable fast data collection over large distances, increasing both spatial coverage and sample density compared to drilling or stake/hotwire transects. Both methods were developed in connection to SHEBA (Eicken et al., 2001; Sturm and Holmgren, 2018) but used for the first time to obtain combined measurements of snow depth and sea ice thickness for repeated transects during Norwegian Young Ice Expedition (N-ICE) from January to June 2015 (Rösel et al., 2018). N-ICE transects were partially done separately over FYI and SYI. The sampling was predominantly over level ice on four separate ice floes, as the sampling sites were drifting continuously into the marginal ice zone and had to be abandoned. These transect lines were about 300 m, with snow sampled at 1–5 m spacing. The GPS positions from N-ICE transects were not precise enough to co-locate snow and total ice thickness values, and ice thickness was approximated by subtracting the means of the probability distribution functions of both measurements. N-ICE drift tracks are also depicted on **Figure 1**.

2.2. MOSAiC sampling equipment

Before describing the MOSAiC sampling techniques we first detail the snow depth probe and the EM device used for transect sampling at MOSAiC.

2.2.1. Magnaprobe snow depth probe

The snow depth measurements along the transects were collected using an automated snow depth probe (**Figure 2a**); i.e. Magnaprobe by SnowHydro LLC (Sturm and Holmgren, 2018). The Magnaprobe is equipped with a data logger that records snow depths, GPS coordinates, measurement timestamps, and several other auxiliary

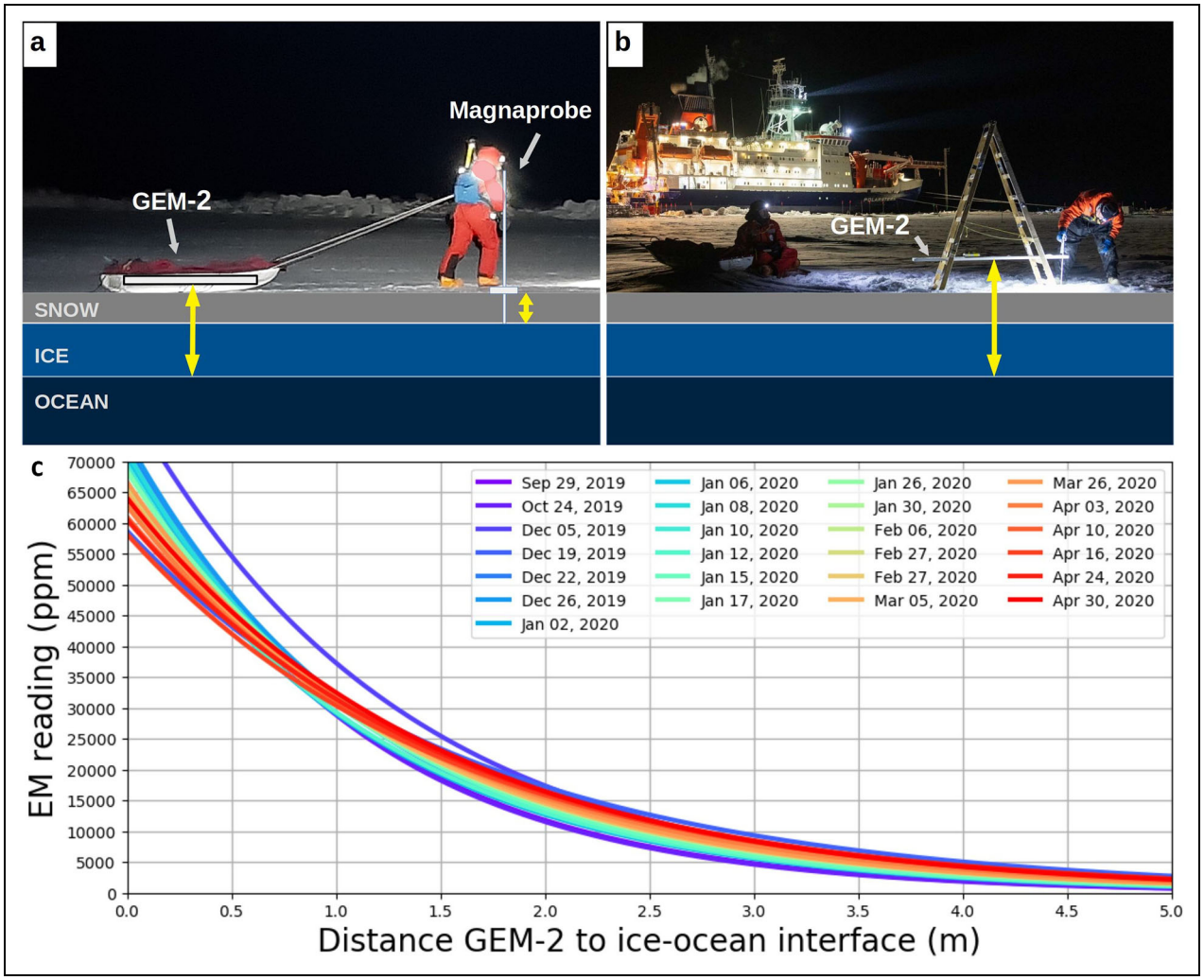

Figure 2. Transect measurements during polar night at the first MOSAiC Central Observatory. (a) Operating the GEM-2 and Magnaprobe (photo: Markus Beck). Magnaprobe measures snow depth by recording the distance between a basket floating on the snow surface and the hard snow–ice interface. GEM-2 measures the strength of the secondary magnetic field which can be used to estimate distance from the instrument to the ice–ocean interface. (b) Calibration of GEM-2 (photo: Marcel Nicolaus). (c) All calibration curves for 18-kHz Inphase channel for the first MOSAiC CO.

data, enabling collection of about 1000–1500 point snow depth measurements per hour. The maximum snow depth measurable by Magnaprobes is 1.2 m. The precision of the measurement depends on the softness of the air–snow and snow–ice interfaces, but as a rule in winter the uncertainty does not exceed 0.01 m. In melting conditions over sea ice, melting snow and the surface scattering layer (SSL) of melting sea ice (Light et al., 2008) are indistinguishable in Magnaprobe measurements (Webster et al., 2022). Therefore, they are combined into one category: snow/SSL. During the melt season on MOSAiC (June–September 2020), the instrument was adapted to measure melt pond depth, and the surface type was manually noted to distinguish between snow/SSL and melt pond measurements (Webster et al., 2022). The Magnaprobe is standard equipment widely used in terrestrial and sea ice snow data collection and, as a direct snow depth measurement, does not need any processing beyond quality control and removal of erroneous data.

2.2.2. GEM-2 electromagnetic induction device

The distance from the snow surface to the ice–ocean interface was measured using the electromagnetic induction (EM) method (**Figure 2a**). This distance includes the combined thicknesses of the sea ice and snow layers and is commonly referred to as “total thickness” (e.g., Eicken et al., 2001; Hunkeler et al., 2015b). On MOSAiC transects, we used a broadband EM instrument sensor (GEM-2 by Geophex Ltd) towed on a small sled. The instrument includes a real-time data processing unit, including a GPS receiver which communicates with a field PC that operates the sensor and records the EM and GPS data streams. The GEM-2 is a broadband sensor that can transmit multiple configurable frequencies in the kHz range simultaneously and record the EM response of the ocean at a sampling rate of 20 Hz. The sensor setup during MOSAiC used 5 frequencies with approximately logarithmic spacing throughout the frequency range of the sensor (1.525, 5.325, 18.325, 63.025, and 93.075 kHz).

During the transect surveys, the sled with the GEM-2 was towed more than 2 m behind the surveying team to avoid an EM response to any other electrically conductive material than the sea ice and ocean layers. Actual GEM-2 sensor data will differ from the ideal response due to sensor drift and specific characteristics of the GEM-2, namely a bias introduced by passive bucking (bucking bias) that is described in Hunkeler et al. (2015a). For this study we used the EMPEX (empirical exponential) approach (Pfaffling et al., 2007) to derive total thickness from the raw frequency response data. The EMPEX method directly relates the in-phase and quadrature components, the real and imaginary parts of the complex EM response to total ice thickness. While this approach can be applied to all frequencies, we used only the 18-kHz in-phase channel in this paper to compute total thickness (**Figure 2c**). The 18-kHz channel has a higher signal-to-noise ratio than the lower frequencies due to greater sensitivity to changes in the electrical conductivity in the sea ice layer, in addition to changes in total ice thickness. In rare cases, when the 18-kHz in-phase channel malfunctioned, we used the 63 kHz quadrature channel, which gave similarly accurate measurements.

Sensor calibrations and verifications were a routine part of the transect observation program carried out immediately before or after the surveys. The GEM-2 was placed at known heights above the sea ice surface using a wooden ladder on top of level ice with a known thickness determined by five drill holes (**Figure 2b**). Because sea ice conductivity changes seasonally (**Figure 2c**), the closest-in-time calibration result was used when a GEM-2 survey was not accompanied by a calibration. This approach is especially important for distance ranges below 2 m where seasonal changes are largest. Special care was also taken to ensure that the GEM-2 was at the ambient temperature before starting a survey, to minimize sensor drift during the survey, and whenever possible that it was placed on the same spot before and after the transect activity to monitor any residual sensor drift. Our EMPEX implementation can therefore be expected to have considerably reduced the impact of sensor drift or miscalibration, and be independent of the GEM-2 bucking bias.

Using a direct relationship between total thickness and in-phase data is based on the assumption that the sea ice conductivity is negligible and the ice–water interface is constant within the GEM-2 footprint, which we approximated as 4× the total ice thickness, after Reid and Vrbancich (2004). While this assumption is reasonable for level ice, the peak thicknesses of ridges are known to be underestimated by as much as 50% (Pfaffling et al., 2007). However, numerical modelling implies that the average of thicknesses recorded across the full width of a ridge including its flanks accurately represents the true mean ridge thickness (Hendricks, 2009).

The total thickness from the GEM-2 calibration and survey data was retrieved shortly after each profile. These quicklook data were later fully quality-controlled during the full dataset review. Here we used all GEM-2 data co-located with Magnaprobe snow depth information. Additional GEM-2 data were collected during MOSAiC by pulling the sled with a GEM-2 with a snow machine. However, without Magnaprobe data, sea ice thickness cannot be estimated from the GEM-2 total thickness observations and thus these GEM-2 datasets have been excluded from this study.

2.3. MOSAiC data sampling strategies and locations

At MOSAiC, we collected snow depth by Magnaprobe and total thickness by GEM-2 throughout a full year from October 2019 to September 2020. The majority of the transect lines fell within 1-km distance of the RV *Polarstern*. From December 2019 to February 2020 sampling was done by skiing; otherwise the sampling group walked. Our overarching strategy was to sample snow depth and ice thickness with sufficient spatial and temporal resolution to resolve their variability. The locations of these transects were selected using the following criteria:

1. Repeatability. Most of the data were collected repeatedly along marked transect lines to create time series. The frequency of repeats was governed by expected rates of change, ambient conditions (light, weather), and purpose of the line.
2. Representativeness. The sea ice cover sampled had to be representative of the CO, and, if possible, of the broader area surrounding it.
3. Co-location. The line had to be close to other measurements made on the expedition, but not interfere with them.
4. Safety and logistics. The surface had to allow early initiation and continuity of the sampling. It had to be safe for the personnel and close to the base.

Following these criteria, several transect lines were established at the three COs of MOSAiC. In total over 87,000 Magnaprobe snow depth measurements and over 167 km of GEM-2 tracks were collected. The horizontal spacing of measurements was typically 1–3 m, depending on the surface and type of transect line. An overview of transect labels, locations, timeline, snow depth sampling spacing, and line length and line geometry is given in **Figure 3**. The snow/SSL and melt pond depth of summer transects (second and third CO) were analysed in detail by Webster et al. (2022). Analysis of the ridge transects is beyond the scope of this paper but will be presented in future. All transect data with metadata are published in PANGAEA repositories (Itkin et al., 2021; Hendricks et al., 2022). More details on the transect lines used in this paper and beyond are given in Text S1.

2.4. Gridding of the data

Sea ice thickness can be calculated by subtracting snow depth (Magnaprobe measurement) from total thickness (GEM-2 measurement). To achieve an accurate calculation, both variables need to be estimated at the same location, and, because sea ice is usually drifting, the same time. As the transect observations were collected repeatedly and are necessary for interpreting other measurements in the CO, the simplest solution for this problem is

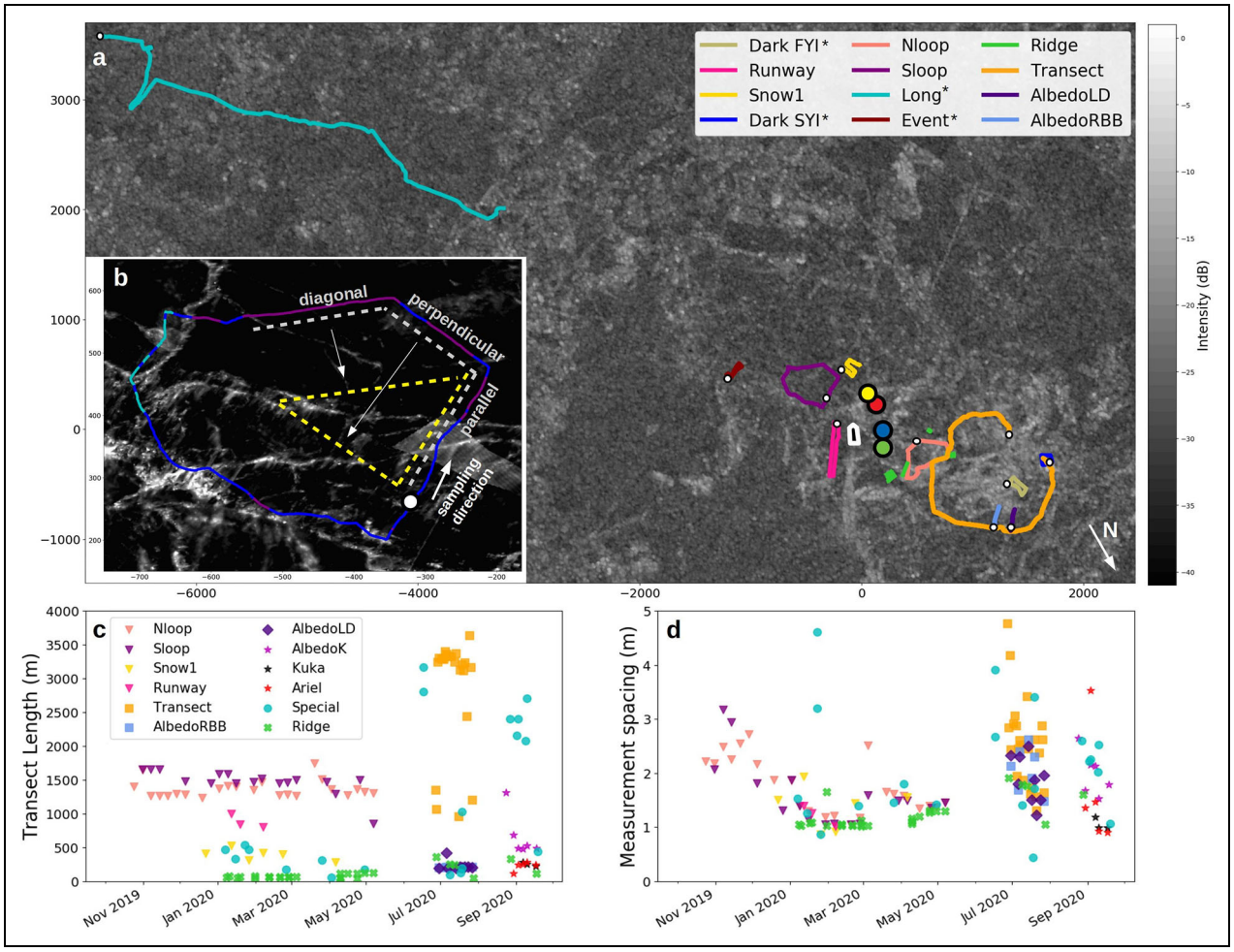

Figure 3. Overview of locations, length and sampling spacing of the MOSAiC transect lines. (a) Maps of transects at the first and second Central Observatories (COs). (A map of the third CO is on Figure S1.) The distance unit of the maps is meters. The transect lines have been drift-corrected to overlay on the *Polarstern's* location in January 2020. RV *Polarstern* is located at the origin of the coordinate system (0,0) and is marked by a white ship contour. The ship's heading in October 2019 (approximately south-southwest) determines the orientation of the map. The areas designated Met City, Remote Sensing site, Ocean City and Remotely Operated Vehicle observatory are marked by yellow, red, blue and green circles, respectively. The start of each transect is marked by a white dot. Transects labels are provided in the inset legend, those annotated by "*" are also called "Special" transects. The background is a Radarsat-2 SAR image from December 31, 2019 (provided by NSA/KSAT through Canadian-Norwegian Radarsat agreement). The brighter features on the Radarsat-2 image correspond to deformed ice and second-year ice (SYI). Dark features are level SYI and first-year ice (FYI). (b) Close-up of the Southern transect loop (Sloop). The background is quick-look of surface elevations derived from the Airborne Laser Scanner (credit: Stefan Hendricks and Arttu Jutila, AWI). The color of the loop track is purple, blue, and cyan for level ice, rubble and ridges, respectively. The "triangle" over level ice used in the spatial analysis is marked by grey (original positions) and yellow (re-arranged positions) dashed lines. (c) Transect length and (d) spacing of snow depth sampling for all three COs. The Long transect on January 23, with a length of 5196 m, is off the axis on panel c.

to construct a local coordinate system and re-project all measurements to it. We selected a projection with its origin at the location of RV *Polarstern* with the ship's heading in October 2019 as its vertical axis. The position of RV *Polarstern* was estimated using the "FloeNavi" system (Nicolaus et al., 2022) a network of several GPS stations deployed on the ice with known relative position to the ship. This method worked well for the period October 2019 to May 2020. Later in the season, the relative motion of individual ice floes in the CO was so strong that the FloeNavi network was not serviceable, and the position of the transects thereafter was estimated based on the ship position only, while the rotation was estimated manually. The locally re-projected transect tracks were then used for mapping, line length, and snow depth measurement spacing calculations like those shown in **Figure 3c** and **d**. Sporadic failures in GPS position recording from the Magnaprobe and GEM-2 and imprecise GPS positions caused unrealistic transect line lengths in places.

The co-location of snow depth and total thickness measurements included several steps:

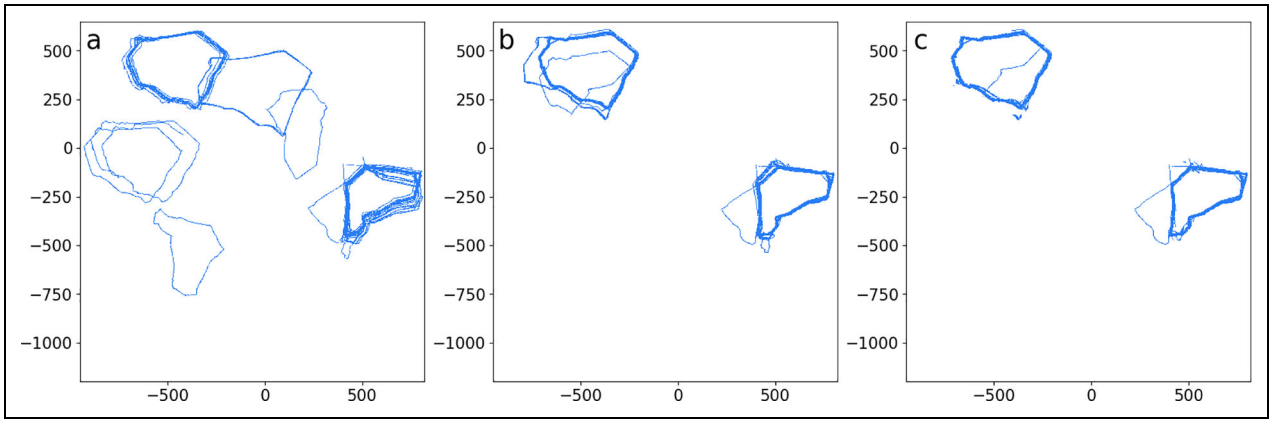

Figure 4. Transect track matching for data from October to May. (a) Original tracks in local coordinate system, (b) translated and rotated tracks, and (c) tracks adjusted to account for the relative motion by sea ice deformation. The transect tracks were manually translated laterally to obtain the closest match to a reference date in mid-January. Most of the discrepancies were due to absolute location errors, which caused lateral shifts and rotation inside the coordinate system. In addition, deformation of sea ice cover had to be reconstructed by careful adjustment of unaffected track pieces.

1. Co-location of snow depth and total thickness data for individual transect lines. Magnaprobe GPS tracks have relatively large absolute bias in location compared to the GEM-2 GPS tracks. Both measurements were normally done near-simultaneously with some 10 m or 20 s offset. The shapes of both tracks were very similar, but the Magnaprobe track location was less stable in week-by-week comparison than the GEM-2 track. The reason for this "random walk" is likely a reduced quality of the Magnaprobe GPS antenna compared to the GEM-2 one. To address this issue we visually inspected and laterally translated all Magnaprobe tracks, so that they would better correspond to the GEM-2 track. The shift was typically 0–10 m (up to 30 m in summer) and was different for each transect.
2. Gridding of the data and sea ice thickness estimation. A grid of 1-m horizontal spacing was created for the CO area, and values of snow depth and total thickness were estimated for individual grid cells using nearest neighbor interpolation. The estimation was done only for the grid cells up to 2 m away from the track. The rest of the cells were not assigned any value. Sea ice thickness was then obtained by simple subtraction of snow depth from total thickness. As the GEM-2 footprint corresponds roughly to 4× total ice thickness (Reid and Vrbancich, 2004), the transect data will necessarily be over-sampled and smoothed over distances shorter than the footprint.
3. Co-location of transect lines in time. To be able to compare the change in time over the same ice cover regardless of drift, positioning error, and deformation, the locations of all repeated transects were additionally examined and adjusted (**Figure 4a** and **b**). A reference date for each transect line was selected. The coordinates of the fixed transect lines changed due to errors in the FloeNavi positioning and more significantly due to sea ice deformation or relative motion of ice floes inside the CO. The former was minor and typically on the order of 0–10 m. As an example for the latter, Sloop drifted by approximately 500 m relative to RV *Polarstern* in mid-November and again by approximately 450 m in April. Additionally there was deformation inside the transect loops themselves, again most notably in the Sloop in November. To co-locate the level parts of the loops throughout the season, sections of the lines were translated and rotated manually to best match their original shapes (**Figure 4c**).

Such procedure accounts for the variable sampling spacing by Magnaprobe (**Figure 3**) and for the data accumulated over the same or very close locations (which typically occurred if the GEM-2 sled was moving very slowly or stopped while measuring). The nearest neighbor interpolation to the grid was selected as the one introducing the fewest artificial values, as the original sampling spacing (1–3 m) was relatively close to the grid spacing of 1 m. Despite large absolute positioning error (e.g., 0–10 m for the GEM-2 track in the local coordinate system), the preservation of the shapes of the transect lines points to very small relative positioning errors in the range of grid spacing.

2.5. Transect profiles

The gridded and co-located sea ice thickness and snow depth were constructed into profiles (cross sections). For data visualization we estimated ice freeboard f_i, the height of sea ice and snow interface over water surface, from sea ice thickness h_i, snow thickness h_s and their respective densities ρ_i (882 kg m^{-3}) and ρ_s (313 kg m^{-3}), with both constants taken from literature values in King et al. (2018), following the hydrostatic equilibrium equation as in Forsström et al. (2011):

$$f_i = h_i \frac{\rho_w - \rho_i}{\rho_w} - h_s \frac{\rho_s}{\rho_w}$$

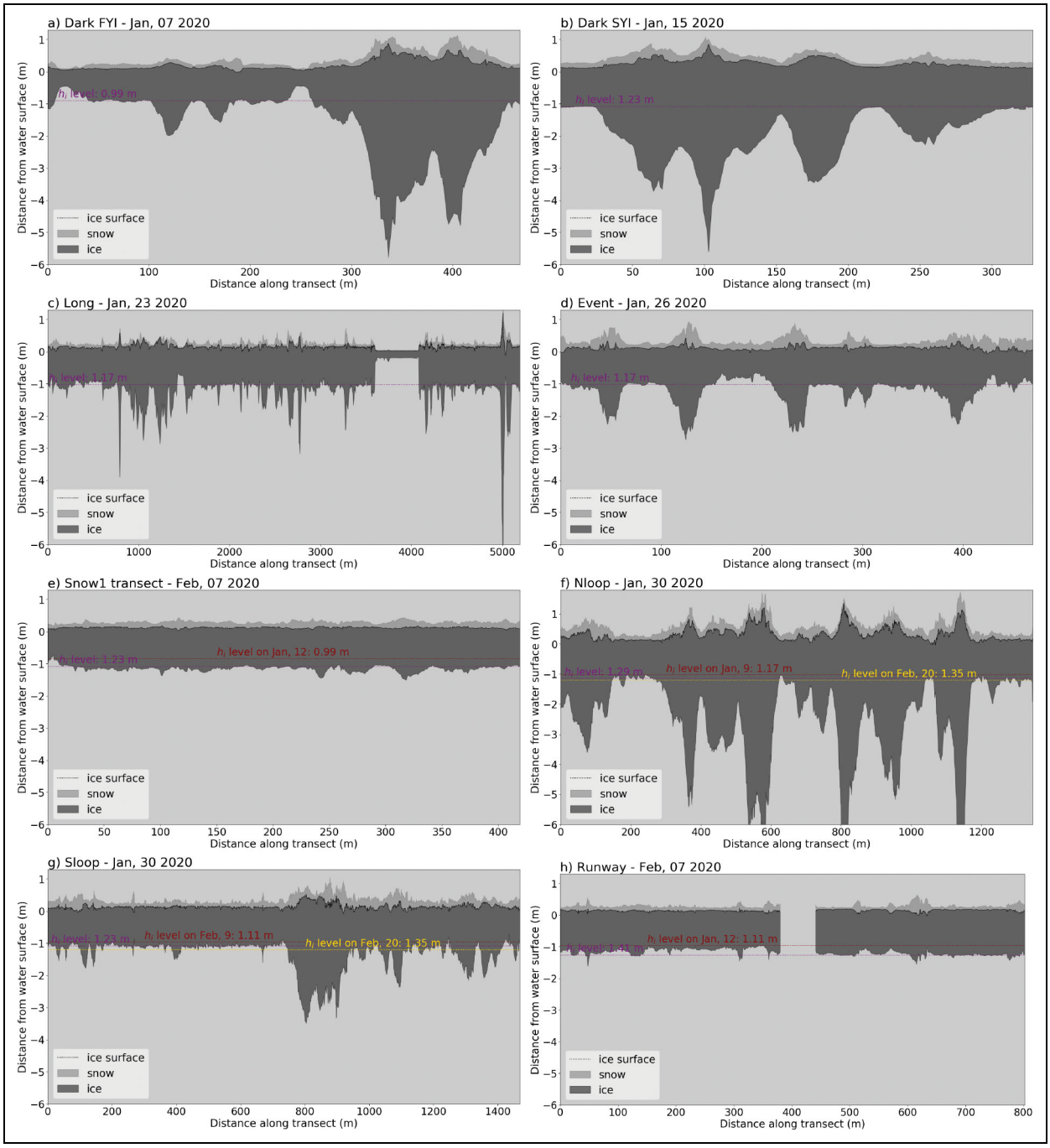

Figure 5. Sea ice and snow transect data represented as profiles for various lines from January–February 2020. Data profiles for the transects (a) Dark FYI, (b) Dark SYI, (c) Long, (d) Event, (e) Snow1, (f) Nloop, (g) Sloop, and (h) Runway. Level ice thickness (h_i level) was estimated by the statistical mode of the sea ice thickness distribution. Note that transects are of diverse lengths, which affects the visual impression of ice roughness. Vertical axis displays snow depth as positive and sea ice thickness as negative values, with water level as zero. Horizontal axis represents distance along the transects. The start of each transect is marked on **Figure 3a**.

While such freeboard estimates tend to have a local bias, they give a satisfactory impression of the surface roughness on the plots so that level ice can be distinguished clearly from deformed ice and leads. Level ice thickness has been determined previously as the statistical mode of the ice thickness distribution (Haas et al., 2017). In our study, we estimated the mode by binning sea ice thickness values between 0 and 2 m into 6-cm-wide bins. We did not find level ice exceeding 2-m thickness in any of the COs. Visual comparison of the transect profiles and such statistical mode and level ice thickness estimates gave satisfactory results (e.g., **Figure 5**).

2.6. Spatial heterogeneity analysis

Previous publications demonstrate that late winter and spring snow depth over level ice are typically autocorrelated at spatial length scales ranging from approximately 5 to 20 m (Iacozza and Barber, 1999; Polashenski

et al., 2012; Liston et al., 2018). Snow dunes are not circular features, but rather elliptical, with axis alignment coinciding with the prevailing wind direction (Iacozza and Barber, 1999; Liston et al., 2018). Consequently, their spatial correlation lengths are anisotropic and depend on the angle at which a transect line intersects such a shape. Samples of length more than 100 m should be sufficient to contain several snow dunes. Here, we analyzed the seasonality of snow depth and ice thickness spatial patterns and used the advantage of co-located data to examine if any potential spatial length scales correspond.

Sloop, which was one of most long-lived winter transects and included substantial level ice surfaces, was selected for this analysis. The total length of the continuous level ice segment in Sloop was 700 m. This segment was not a straight line, and if re-organized in space, formed a right-angle triangle with sides 260 m, 180 m and 260 m long (see triangle with yellow sides on **Figure 3b**). For simplicity we named the triangle sides according to their orientation in relation to the ship heading: parallel, perpendicular and diagonal. While these level ice transect and segments are relatively short, they are substantially longer than previously documented lines by Iacozza and Barber (1999), Sturm et al. (2002a) and Liston et al. (2018), where individual straight segments were even shorter, at 100 m (Iacozza and Barber, 1999; Sturm et al., 2002a; Liston et al., 2018), or the snow sampling distance was large, at several meters (Sturm et al., 2002a).

To evaluate the spatial heterogeneity of snow depth and ice thickness in level ice segments of the transects, we applied discrete Fourier transform (DFT) to the gridded transect data. We argue that DFT is a more suitable method than the semi-variograms previously used for such analysis (Iacozza and Barber, 1999; Liston et al., 2018), as it can indicate more than one correlation length peak and provides a simple statistical confidence test. The DFT was applied using python-scipy package Fast Fourier Transform (Cooley and Tukey, 1965; Virtanen et al., 2020). The data in the real part of the spatial frequency domain were then used to determine the correlation length scales of the data. To avoid edge effects, all segments were continuous and the analysis frequency corresponded to the shortest segment length. To estimate the statistical significance of peaks in the Fourier power spectrum we tested the null hypothesis that our data differ from white and red noise. While the power of white noise is constant, at red noise the power decreases with frequency (increases with wavelength) and is typically used to estimate confidence levels in geophysical time series that are auto-correlated. Here we used a simple univariate lag-1 auto-regressive AR(1) process following Torrence and Compo (1998). After a DFT all frequency values were converted to wavelength to allow the interpretation of the spatial length scales. To construct the statistical confidence levels for the entire season, all sampling time steps per triangle side were accumulated. As snow depth and ice thickness both increase through the season, we subtracted the means at each time step. Only then were the AR(1) properties extracted.

The transect data also covered pressure ridges and other deformed ice (cracks, lead edges, ice rubble). Samples of these features in the transect data were too small to derive their geometrical characteristics statistically. Instead, we estimated from qualitative field observations that a rough ice surface impacts snow accumulation over a distance of approximately 50 m. This estimation means that snow drifts caused by a ridge sail extended approximately 25 m to each side of the sail crest.

3. Results and discussion

3.1. Similarities between ice types

The data presented in this paper were collected predominantly over SYI. Because sea ice in the Arctic, and especially in the Transpolar Drift, is now composed mainly of FYI (Kwok, 2018; Stroeve and Notz, 2018), a different sampling strategy would have been desirable to acquire representative data. Collecting data over FYI at MOSAiC, however, was difficult due to two reasons: (1) newly grown FYI was too thin to ensure a safe working platform during freeze-up; and (2) even after freeze-up, FYI remained weaker than surrounding older ice and was undergoing frequent deformation that made repeat transects difficult. All transect lines on FYI that were started in January were destroyed by sea ice deformation in February and March. For a short period in January and early February, however, when sampling conditions were most stable, we sampled over various ice types in the first CO and its vicinity. The resulting comparison is presented in **Figure 5**.

Regardless of ice age, by January the level sea ice thickness on all transects was very similar at around 1 m (between 0.99 m and 1.23 m). That period had stable freezing temperatures and high ice growth rates (Katlein et al., 2020), so the level sea ice thickness steadily increased throughout the month at all locations that were remeasured (see multiple level ice thicknesses on **Figure 5e–g**). The Runway transect profile (**Figure 5h**) also gives clear evidence that under thin snow, sea ice grew thicker. This transect was sampled along both sides of the emergency runway, where one side (distances greater than 400 m on the figure) had very little snow (on average less than 5 cm). This side had the thickest level ice of all transects in February. Because the thermal conductivity of snow is an order of magnitude smaller than that of sea ice, modeling studies (e.g., Notz, 2009) have suggested that FYI, which tends to have thinner snow cover due to a shorter accumulation period than SYI, should grow to a similar thickness as SYI covered by much thicker snow by the end of winter. Such relationship was observed before (Rösel et al., 2018), but not this early in the season. The Long transect is an example of a transect over mixed ice ages (**Figures 3** and **5c**) where the level ice thickness is similar over the whole transect length (except over the refrozen lead) despite differing ice ages.

The difference in snow depth between FYI and SYI transects persisted beyond February, but was very similar at the end of the growth season. The FYI transect Runway was unfortunately lost in deformation events in March, making continuous comparison of snow accumulation on different ice ages impossible. The initial surveys on

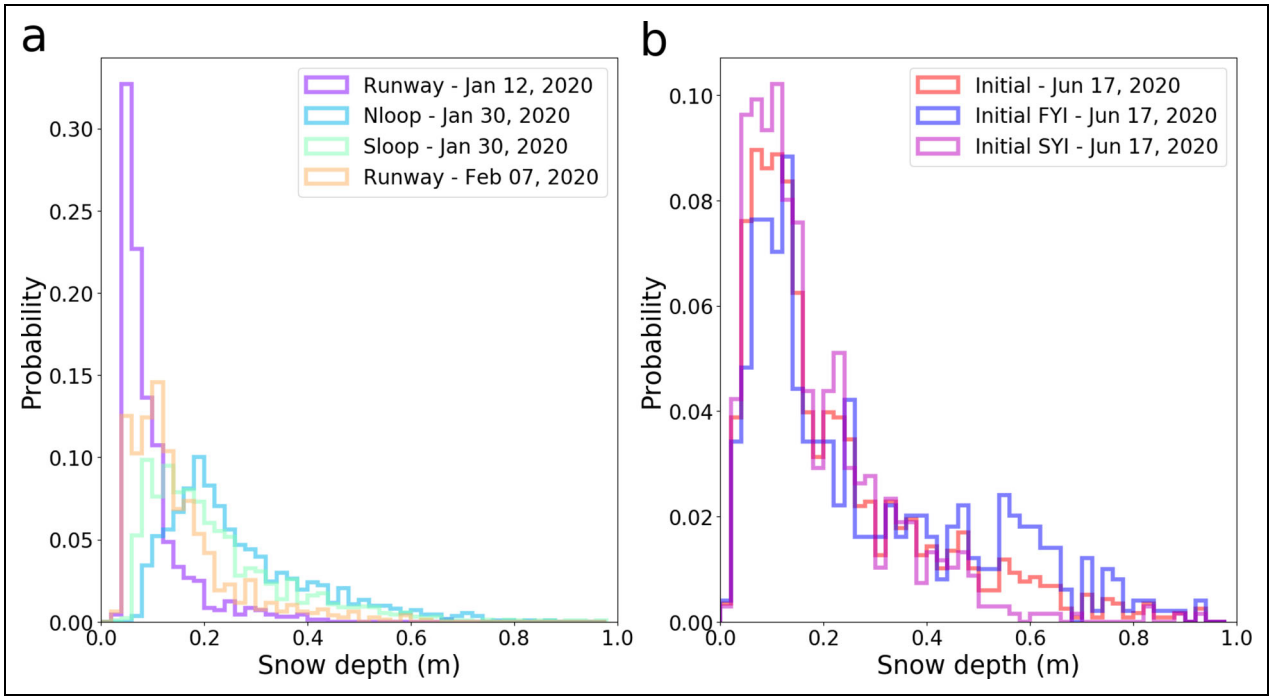

Figure 6. Snow depth probability density functions for winter and spring transects at MOSAiC. Transects in (a) January–February and (b) June 2020 over first-year ice (FYI) and second-year ice (SYI). The bin width in histograms is 2 cm. The division between SYI and FYI for June roughly follows Webster et al. (2022). Data sample size for the June transect was 1184, where 498 measurements were taken over FYI and 686 over SYI.

June 17 sampled the second CO after rapid snow melt had begun. That survey closely resembled the later established repeat transect at the second CO over predominantly deformed SYI and FYI. Based on Webster et al. (2022) we split the initial survey into predominantly SYI and FYI parts and found no difference in the FYI and SYI modal snow depth or statistical distribution (**Figure 6b**). The modal snow depth (just below 0.2 m) resembled the modal snow depth on the Nloop transect in January. As this second CO transect was predominantly on deformed sea ice, further study, e.g. by numerical models (Liston et al., 2018), is needed to confirm that snow depth was similar across all ice types at the end of the accumulation season.

3.2. Seasonal time series

Although continuous sampling over the same ice cover was not possible for the whole duration of MOSAiC, the sea ice transects sampled at each of the three COs are comparable in snow depth and sea ice thickness and can be stitched into a seasonal cycle. The first CO covers most of the ice growth and accumulation period from October 2019 to May 2020. The second CO from June to July 2020 covers the melt period and early summer. The third CO from August to September 2020 covers the transition from summer melt into fall freeze-up. Even though the third CO data were collected last, they represent the logical start of the sea ice and snow life cycle.

The MOSAiC seasonal cycle of snow (**Figure 7a**) shows how a snow cover begins to accumulate in September on remnant FYI (now SYI). These measurements were made at high latitudes (north of 85°N; **Figure 1**), whereas further south, snow may not accumulate until later in the season due to differences in radiation, air temperatures, and precipitation phase. The late summer/early autumn snow cover is unstable and may vanish with warm air intrusions and rain, but by the start of the first CO in October air temperatures were stably below the freezing point and snow had started to accumulate. By the beginning of October, all SYI except refrozen melt ponds was covered by snow (**Figure 8b**). After October 8, melt ponds were also snow-covered (**Figure 8c**). During this late freeze-up time new FYI continued to grow in large leads that opened inside the pack ice (**Figure 8d**). There, snow started accumulating only in November. End of October snow cover accumulation, however, was slow on all ice types, averaging 0.01, 0.05 and 0.01 m month^{-1} on transects Nloop, Sloop and Snow1, respectively. Assuming snow accumulation on transect Runway in the beginning of October, snow accumulation there was 0.03 m month^{-1}. Afterwards, the first noticeable increase in snow cover depth occurred in February. The increase was especially noticeable for level ice on the Snow1 transect (0.10 m month^{-1}) where the standard deviation also rose abruptly. At that time, FYI transects became inaccessible and there were no further measurements over FYI. However, because Snow1 and Runway transects were both predominantly level ice and very close in mean and standard deviations at the beginning of February, they very likely remained so at end of February. Therefore this February snow depth increase was very likely the event that evened the snow depth across all ice types. At the same time, mean snow depth and standard deviation reached their peak values at or just shy of 0.3 m and 0.12–0.2 m, respectively, then remained

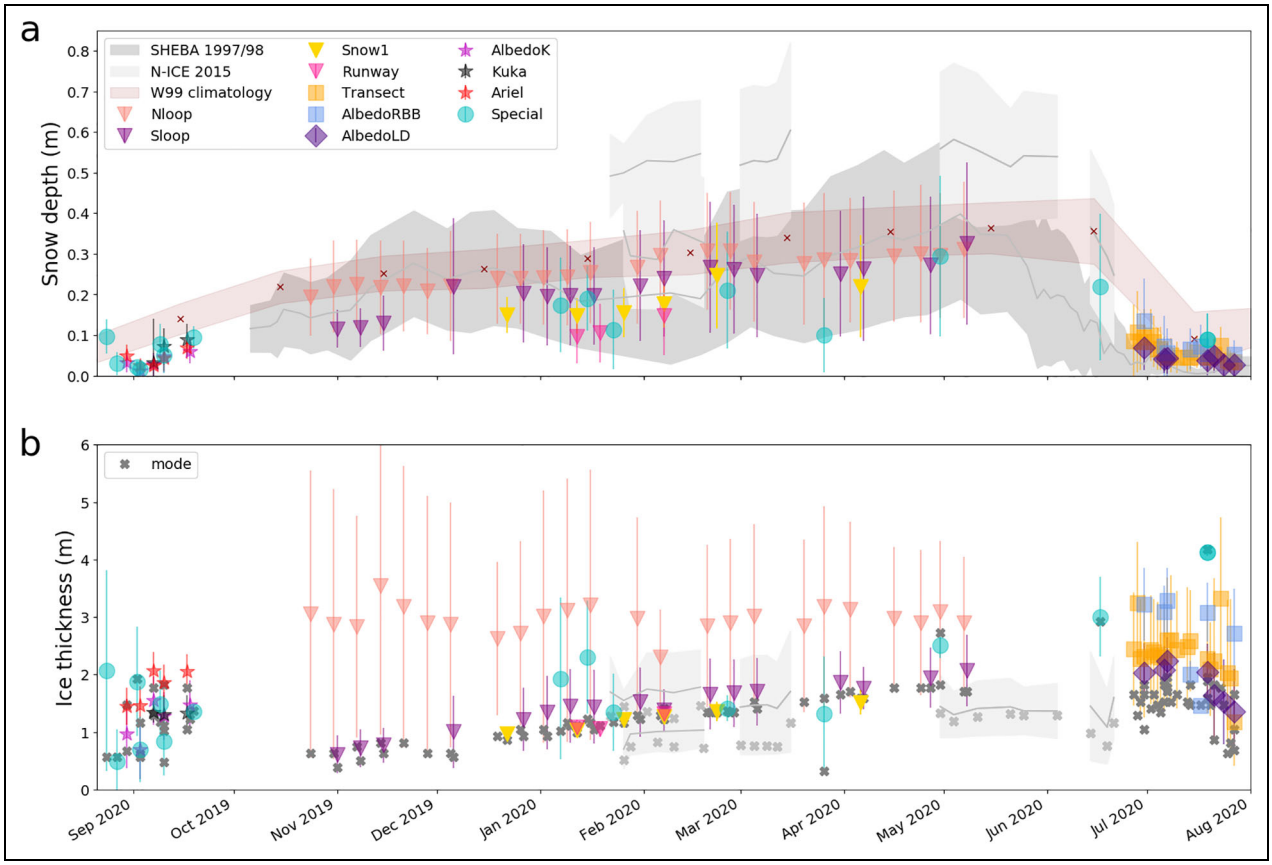

Figure 7. The seasonal cycle of snow depth and ice thickness constructed from Central Observatory transects. The means, standard deviations and modes of gridded repeat transects from the first, second and third MOSAiC Central Observatories constructed into seasonal cycles of (a) snow depth and (b) ice thickness. Note that the beginning of the annual cycle was collected last (third Central Observatory) and that there are three separately sampled but similar ice surfaces used to construct the full annual time series. Data sample sizes can be estimated from **Figure 3c** and **d**. Snow data from previous expeditions (SHEBA, N-ICE) and climatology are also shown (with standard deviations as wide grey belts). Sea ice transect data were collected only at N-ICE. Where N-ICE data is double, both FYI and SYI data were collected. The thinner of these two datasets was collected over FYI.

around these values until the last measurements in the first week of May.

The last measurements at the first CO were followed by over a month-long gap in observations due to vacating the floe for a personnel rotation. The melt onset began in late May, followed by freezing conditions and substantial snowfall in early June (Webster et al., 2022). The first measurements at the second CO showed the same snow depth over both SYI and FYI (**Figure 6b**). We did not capture snow melt onset, but captured the gradual decline in snow depth and melt pond evolution in late June and July. The melt rates between June 17 and 30 were -0.29 m month^{-1}. By late July, the average snow/SSL depth fell below 0.05 ($\pm$0.04) m, which is within the thickness range of the uppermost part of the melting ice layer, also called "the surface scattering layer" (Light et al., 2008). The majority of snow had melted away by early-to-mid-July, with the remaining snow being remnants of snow drifts by ridges (Webster et al., 2022).

We compared the MOSAiC snow annual cycle from various transects to historical observations. The climatological monthly means (Warren et al., 1999) and SHEBA annual cycle (Sturm et al., 2002a) both outline the most rapid accumulation phases in the beginning of winter and in spring. Here we note that the SHEBA snow line included a refrozen lead with thin snow cover from January onward (Sturm et al., 2002a). The very large snow depth recorded at N-ICE (Rösel et al., 2018) also accumulated in the early winter (Liston et al., 2018). Across all datasets, the deepest snow cover occurred in May. MOSAiC and N-ICE were both conducted on ice in the Transpolar Drift, while SHEBA was collected on predominantly MYI in the Beaufort Gyre (**Figure 1**). The climatology was collected primarily in the central Arctic. The standard deviation for SHEBA and inter-annual variability of the climatology, however, overlay with the MOSAiC SYI transect line annual cycle, while the MOSAiC FYI snow depth is lower than in any other recorded seasonal cycle.

The MOSAiC seasonal cycle of sea ice thickness (**Figure 7b**) shows a large spread in mean and modal sea ice thickness in late summer (third CO). Some of this sea ice can survive the summer melt and develop into distinctive types of SYI also found at the first CO along the transects Nloop and Sloop. These two ice type subgroups

Figure 8. Panoramic photographs of the first Central Observatory in October 2019. Photos of approximate areas of the transects (a) Runway, (b) Sloop, and (c) Nloop in October when sea ice on the Runway was still forming and the Sloop area still had large surfaces of bare ice, where dark features are refrozen melt ponds. The ice surface of Nloop was ridged ("the Fortress") and is visibly brighter due to newly fallen snow. Panels (a), (b) and (c) are extracted from (d) the Panomax panoramic photo from October 5, 2019 at 4 UTC, and marked by boxes of corresponding colors. (e) Panomax panoramic photo from October 9, 2019 at 4 UTC right after a major snowfall on October 8. Here the contrast between ice types is less visible. (f) Panomax panoramic photo from October 16, 2019 at 4 UTC after a lead opening and ridging. The ice surface in the first Central Observatory continued to deform and new leads and ridges occurred throughout October. The first transect sampling started at end of October. The installations visible on October 16 from left to right are: the Remotely Operated Vehicle observatory hut (relocated to the starting point of Sloop at the end of October), MetCity, Remote Sensing site (relocated closer to MetCity in November) and Ocean City. Panomax panoramic pictures give an approximately 180-degree view from RV *Polarstern* (Nicolaus et al., 2021). After mid-October Panomax pictures are too dark to display.

had contrasting ice growth. The thicker deformed ice of Nloop hardly gained any mean sea ice thickness in winter (growth rate of 0.004 m month^{-1} from November to May) and experienced a gradual decrease in standard deviation (from approximately 2 to 1.2 m). However, the second group, with thinner and more level sea ice types, had growth rates of 0.4, 0.15 and 0.3 m month^{-1} on transects Sloop, Snow1 and Runway, respectively. The large mean growth recorded for Sloop was caused by pressure ridge formation. This difference is also noticeable in the standard deviation, where Sloop had values around 0.6 m compared to about 0.1 m in the level transects (Snow1 and Runway). After an April ridging event in Snow1, standard deviation there increased to 0.2 m. The statistical modes that represent level ice thickness converge to about 1.2 m by the second half of January (as detailed in the previous section and **Figure 5**), when the modes for Nloop, Sloop, Snow1 and Runway were 1.29, 1.23, 1.17 and 1.41 m, respectively. The seasonal growth calculated from the modes was about 0.2, 0.24, 0.17 and 0.33 m month^{-1}. Based on photos of thin ice cover (**Figure 8a**) we assume that FYI was formed approximately on October 1, 2019.

We do not have sufficient measurements in the transect dataset in the early melt season to detect the onset of sea ice melt. Late April and May transect data from Nloop and Sloop indicate that keels of the ridges had started to melt. While a short-lived surface melt event occurred in late May, and continuous surface melt began in mid-June (Webster et al., 2022), level ice started to thin continuously from July 10 on, with melt rates of −1.74 m month^{-1} when comparing means and −2.63 m month^{-1} when comparing modes. These melt rates are preliminary as the GEM-2 data for the melt period have not yet been

calibrated for changes in sea ice conductivity. The GEM-2 thickness data, however, are indirect measurements, and measurements over deformed ice especially can be subject to bias. Values in the Nloop have some small transient increases, which we attribute to large local variability and inaccurate retrievals due to inclination of the instrument inside the sled (Hunkeler et al., 2015b) while traveling over heavily deformed ice in the Nloop.

MOSAiC transect measurements have given the first values for spatially distributed ground truth sea ice thickness for the entire seasonal cycle. Measurements by previous expeditions covered only part of the season (N-ICE), or sea ice thickness was measured only at more spatially confined areas (SHEBA). Because winter air temperatures were comparably low for all three drifting stations (Cohen et al., 2017; Persson et al., 2017; **Figure 9**) and snow at MOSAiC was relatively thin, we would expect sea ice at MOSAiC to be correspondingly thick. At N-ICE, which had over 0.4 m of snow on mixed ice type, modal sea ice thickness remained at about 1 m at the end of the growth season. The hot wire data from SHEBA, from both MYI and FYI locations, show that the mean level sea ice thickness in May was 2.05 and 1.31 m, respectively (Perovich et al., 2003). The SYI modal thickness for Nloop and Sloop of 1.71 m is similar to these values.

3.3. Interaction of winter snow and ice

3.3.1. Spatial scales of correlation of snow and ice

The snow and ice transect data over level ice show a development of spatial self-similarity through the winter season (**Figure 10**). The entire 700-m-long triangular segment over level ice in Sloop (between 0 and 700 m on **Figure 5g**) shows spectral peaks in sea ice thickness spatial correlation length scales (SCLS) concentrated between 20 and 40 m wavelengths, and again between 60 and 90 m wavelengths. Spectral peaks in snow depth SCLS occur at many different wavelengths (**Figure 10b**). These anisotropic signals in ice and snow transects develop or vanish through the season and were analysed in detail separately for each segment of three different directions (see **Figure 3b**).

At the beginning of the winter, the parallel side of the triangle (between 440 and 700 m on **Figure 5g**) had a distinctive spectral peak in sea ice thickness SCLS between 60 and 70 m (**Figure 10c**). This peak vanished in January, when a peak between 20 and 30 m strengthened and persisted until the end of the winter. The signals in snow were less distinct, with most persistent peaks between 20 and 30 m (**Figure 10d**). A large January peak at approximately 70 m was caused by the artificial snow dunes that formed behind the Remotely Operated Vehicle observatory hut. These subsided after the hut was removed, but similar features returned in February as new ridges formed. These new ridges were not part of the transect, but ran parallel to this side of the triangle (at about 20 m distance) and influenced snow accumulation on this part of the transect line. This side of the triangle had high standard deviation and consequently high confidence levels based on the white and red noise, despite high power spectrum.

The perpendicular side of the triangle (between 440 and 700 m on **Figure 5g**) remained level during the entire winter. Here, sea ice thickness SCLS had a spectral peak at 60 m at the beginning of the winter (**Figure 10e**). This peak gradually degraded by mid-January. There was a new mid-winter peak in sea ice thickness SCLS at approximately 35 m, but it also faded by March. The signals in snow SCLS were first transient, but established between 20 and 40 m by March (**Figure 10e**).

The diagonal side of the triangle, 260 m in length, was a completely level segment (between 440 and 700 m on **Figure 5g**) with the lowest snow depth in Sloop. It had no significant spectral peak in sea ice thickness SCLS in the beginning of winter, but transient peaks developed between 15 and 25 m and 35 to 90 m during the second half of the winter (**Figure 10e**). Snow had a number of similar transient peaks during the same period, but also a strong peak between 80 and 90 m that developed from February onward (**Figure 10f**).

Our results show that sea ice thickness had strongest self-similarity SCLS signals in the beginning of winter. These signals were anisotropic and strongest in the perpendicular and parallel directions. Because the Sloop transect was established on previously ponded SYI, these signals clearly originated from the refrozen melt ponds. As the strongest signals in the analysis, they demonstrate the impact of melt ponds on sea ice thickness during the subsequent winter season. Existence of melt ponds can be confirmed by qualitative analysis of the Panomax pictures (**Figure 8**). Another illustration of how the melt ponds can create a repetitive pattern in sea ice cover is visible from an orthophoto map at the third CO (Figure S1).

The signals in snow SCLS were clearly anisotropic. They developed at the end of February, and their geometry did not change afterwards. They were short at perpendicular side (20 to 40 m) and long at diagonal side (80 to 90 m). These lengths were larger than the typical previously observed values for the long and short elliptical axes of snow dunes of between 12 and 50 m (Iacozza and Barber, 1999; Liston et al., 2018), where transect line segments were limited to a 100-m distance or had sampling intervals longer than 1 m (Sturm et al., 2002a). The February storm seemed to be the most critical weather event for the development of the snow cover. The prevailing wind direction at the peak velocities was then northeast (**Figure 9**). In contrast, all other major events that winter had predominantly strong southeasterly winds. The February storm was also the first storm after a prolonged calm period and it brought mild temperatures close to -10°C (compared to more typical winter temperatures of about -30°C). By the time of the February storm the first CO rotated by about 40 degrees and the northeast direction was approximately aligned with the north arrow on **Figure 3**. This rotation made the orientation of the perpendicular and diagonal sides of the triangle approximately across-wind and along-wind, respectively. The short and long snow dune axes therefore correspond with an elliptical geometry.

At the diagonal side that stayed predominantly level and had thin snow during the entire winter, there were spectral peaks in snow depth SCLS matched by peaks in

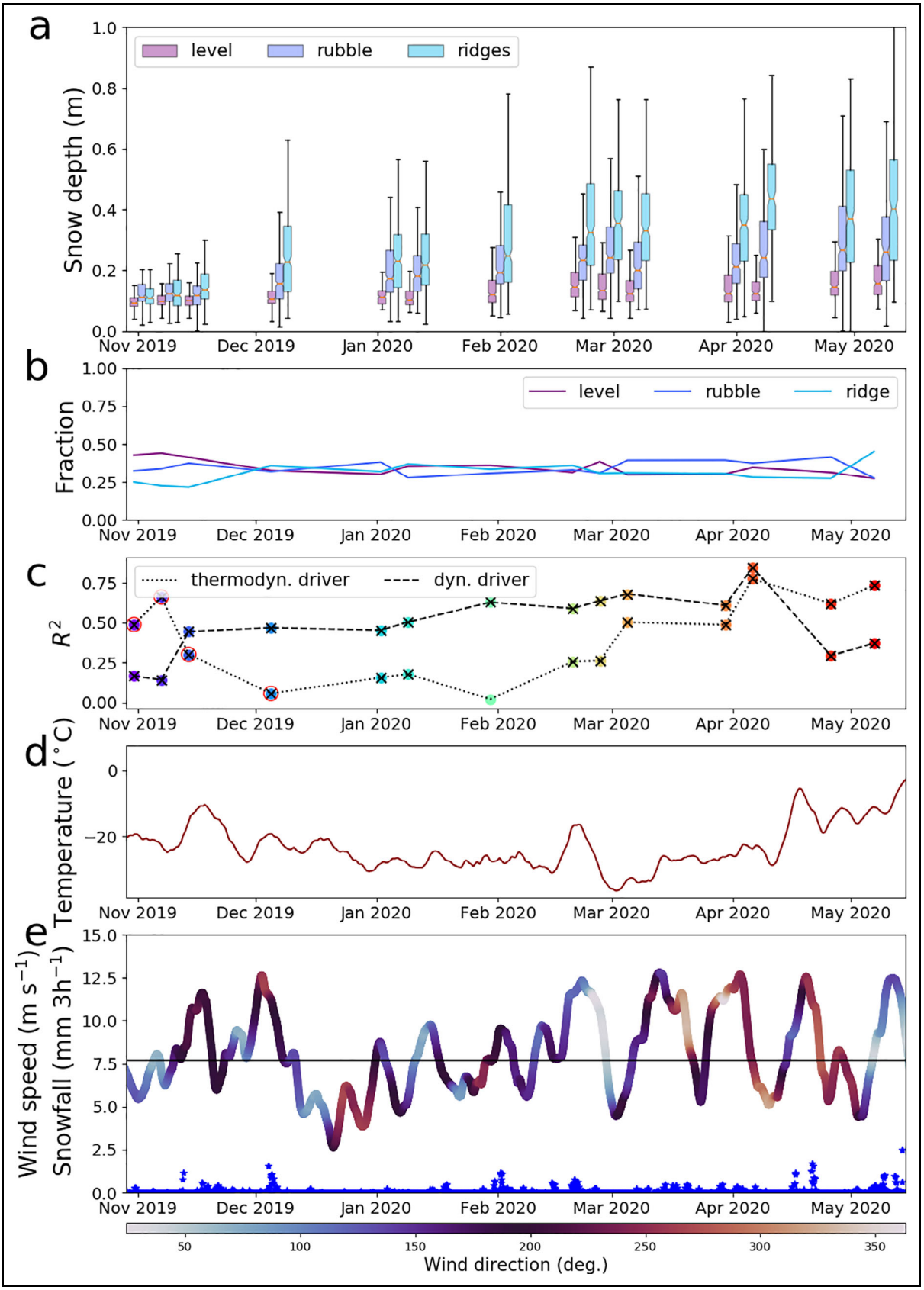

Figure 9. Time series data on winter development and meteorological conditions for transect Sloop. (a) Snow depth distribution on level ice, rubble and ridges; (b) fraction of level, rubble and ridge ice; (c) R^2 or thermodynamic and dynamic drivers (see Section 3.3.2); (d) air temperature at RV *Polarstern* (Schmithüsen et al., 2021a); and (e) wind speed (Schmithüsen et al., 2021a) and snowfall rates (Matrosov et al., 2022; blue stars). Colors in (c) correspond to the ones used for specific dates in **Figure 10**. Red circles on R^2 denote negative correlation. All correlations where the marker has a black cross are statistically significant at 95% confidence levels. Drifting wind events are occasions when the wind speed surpasses 7.7 m s^{-1} (Li and Pomeroy, 1997), marked by a horizontal black line in (e).

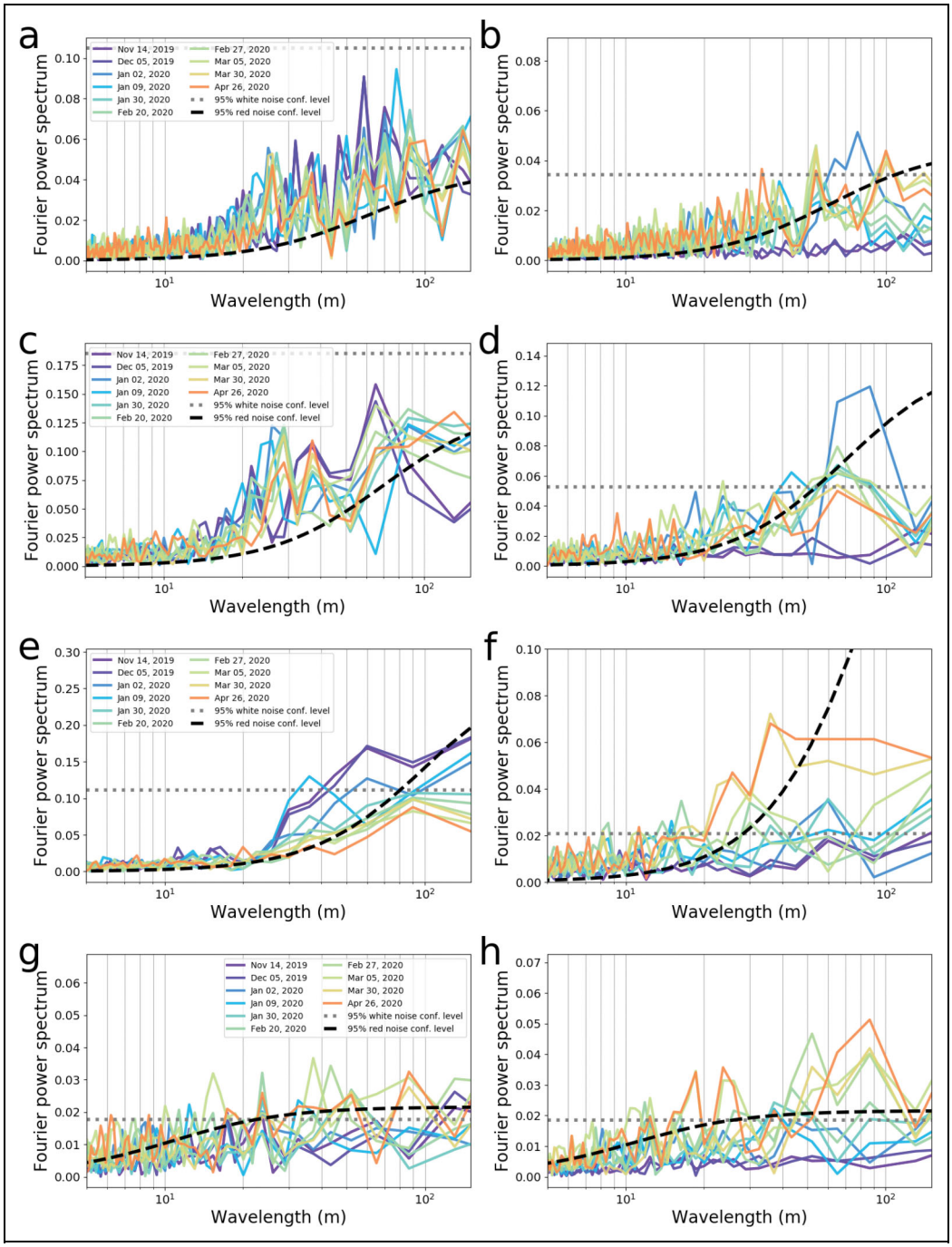

Figure 10. Discrete Fourier transform of ice thickness and snow depth for the level ice of Sloop. Discrete Fourier transform of sea ice and snow for (a, b) entire level ice section (triangle); (c, d) parallel side of the triangle; (e, f) perpendicular side; and (g, h) diagonal side. Only the real part of the transform is shown. The triangle sides are named in relation to the ship heading direction as shown on **Figure 3b**. The grey and black dash lines are the 95% confidence levels for white noise and red-noise AR(1) processes (see Section 2.5).

ice thickness SCLS at end of winter. While this connection was less conclusive at the other two sides, most of the snow and ice segments often show two clusters of spectral peaks that correspond roughly with the long and short elliptical axes of snow dunes. This correspondence suggests that snow depth is the main modulator of sea ice growth and that the patchy snow blanket likely leads to a corresponding geometry in the ice cover.

As described in Section 2.3, GEM-2 data have a large footprint and over-sample the sea ice thickness. Such smoothing has no constraints for our findings, as we found no signals in snow SCLS shorter than 8 m (a GEM-2 footprint corresponding to 2-m level sea ice thickness in May). The 700-m-long section divided into 180- to 260-m-long segments of transect data over level ice is, however, a relatively small sample. All described spatial patterns differ significantly from red noise at 95% confidence levels, although only two features of length scale 90 m fit into a 200-m-long segment. While auto-correlation in snow cover is a visible surface

phenomena that has been documented previously (Iacozza and Barber, 1999; Sturm et al., 2002a; Polashenski et al., 2012; Liston et al., 2018), the periodic features in ice need further investigation by more extensive data or by numerical modeling. We further explore the available MOSAiC data in Section 3.3.3 "Snow accumulation and ice growth."

3.3.2. Sea ice roughness and snow distribution

Data from transects Nloop, Sloop and Snow1 suggest that ice age was not the dominant factor determining snow cover properties at various locations in the first CO. Sloop and Snow1 had the same ice age, but displayed different fractions of deformed ice surface and contrasting mean snow depth and standard deviation until the end of February (**Figure 7**). Also, the profiles in **Figure 6** show more snow accumulation on thick, deformed ice, compared to level ice of modal thickness. To explore this relationship further we used a simple linear correlation of sea ice roughness and snow depth (**Figure 11**). Sea ice roughness can be estimated from the standard deviation of the sea ice thickness over a certain distance of the transect line (Beckers et al., 2015). Here we used a 50-m running window σ_{i50} to estimate sea ice roughness. This distance falls in the middle range of the snow and sea ice patterns found in spectral analysis (**Figure 10**). This distance also coincides with our field observations of how far away from the ridge crest snow depth appears to be elevated. Castellani et al. (2014) found 20 to 70 m ridge spacing in their late winter data for the Central Arctic. Roughness estimated from ice thickness has deficiencies, because variation of sea ice thickness does not necessarily indicate a rough upper surface of ice. For example, variable sea ice thickness could correspond to ridges without sails.

The statistical relationship between σ_{i50} and snow depth developed after the first pronounced drifting snow period and the November ridge formation (**Figure 9**). We defined the drifting snow periods as times when the wind speeds surpassed the 7.7 m s^{-1} threshold value, after Li and Pomeroy (1997). The square of the Pearson correlation coefficient R^2—a measure of the fraction of variability of a dependent variable explained by an independent variable, increases to about 40%. Here we call this relationship the "dynamic driver" of snow distribution on sea ice. This driver then remains high through the period without new deformation in the loop and reaches 85% in early April. Afterwards, this relationship weakens, likely due to the occurrence of new cracks, leads and ridges in the transect loop.

Field-data-constrained numerical model simulations for the N-ICE2015 case (Liston et al., 2018) showed that ridges captured about 22% of all snow cover. For SHEBA, Sturm et al. (2002a) reported that only 3%–6% of snow was in ridge drifts, but the ridge fraction in the SHEBA snowline was small. For MOSAiC, Sloop transect surfaces over level, rubble and ridge sea ice were approximately evenly distributed and each roughness class took about one third of the surface. Threshold σ_{i50} values 0.1 m of for rubble and 0.3 m for ridges were used to separate between these roughness types, corresponding with the observer's perception of these features. The amount of level ice decreased over the season, while rubble and ridges increased (**Figure 9**). These findings correspond to the long term trends observed in the Fram Strait, which show that about one third of sea ice exiting from the Arctic is deformed (Hansen et al., 2013).

In environments with relatively little snow, as on MOSAiC, relatively small roughness features can capture

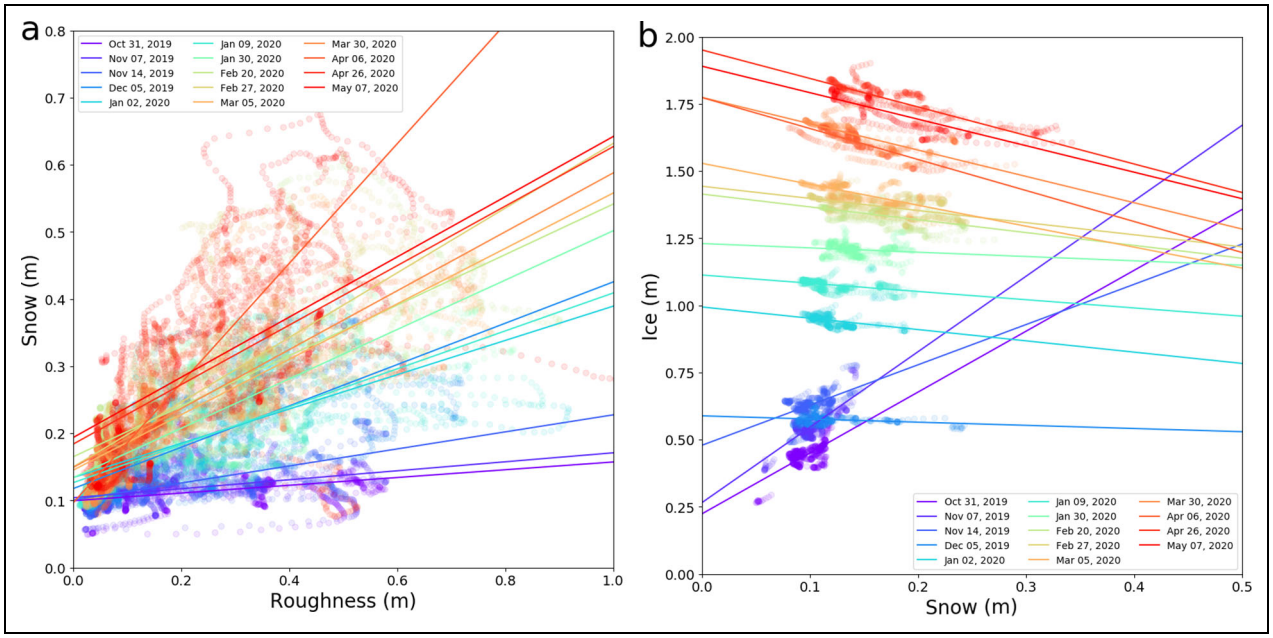

Figure 11. Scatter plots of dynamic and thermodynamic snow–ice interactions. Data for (a) snow depth versus ice roughness and (b) ice thickness versus snow depth. All correlations are statistically significant at 95% confidence levels.

significant amounts of snow. For example, in the beginning of April (**Figure 11a**), when smooth level ice ($\sigma_{i50} = 0.05$) accumulated only 0.14 m of snow, the ice surfaces with $\sigma_{i50} = 0.2$ m (rubble and lead edges) captured double that amount (0.27 m), and ice surfaces with $\sigma_{i50} = 0.6$ m (large ridges) accumulated on average nearly five times the snow depth as level ice (0.63 m).

The MOSAiC time series of mean snow depth and its standard deviation for separate classes of level ice, rubble and ridges (**Figure 9**) show that ridges especially continued to accumulate snow on a weekly basis, while the mean snow depth on level ice increased more slowly and even decreased in periods with strong winds and little precipitation. These findings indicate that snow was eroded from level ice and deposited in ridges. There are periods, however, when snow depth decreased in rubble and in ridges. These periods in January and March witnessed strong deformation and lead opening in the vicinity of the first CO (Nicolaus et al., 2022) and some of the snow was likely removed into those leads and newly formed ridges. At the end of April, on the last complete sampling of Sloop, level ice occupied 31% of surface and captured only 18% of snow volume (**Figure 9**). Rubble and ridge roughness classes in turn occupied 41% and 27% of the transect line, and accumulated 45% and 36% of the snow volume, respectively. Using a different approach Webster et al. (2022) found that, on average, snow drifts on deformed ice covered about 16% of the transect at the third CO and contained 33% of the surveyed snow by mid-July.

3.3.3. Snow accumulation and ice growth

As shown in Section 3.3.1, snow cover is uneven on level ice and can likely cause corresponding heterogeneity in sea ice cover. Because of thermal properties of snow (Maykut, 1978; Sturm et al., 2002b; Persson et al., 2017; Provost et al., 2017), the uneven snow distribution should cause spatially heterogeneous conductive heat fluxes and ice growth on level ice, resulting in thin sea ice under thick snow and vice-versa (Sturm et al., 2002b). This effect can be referred to as the "thermodynamic driver" of ice thickness distribution under snow. In late summer and freeze-up, this relationship is commonly the opposite (Lee et al., 2011; Arndt and Nicolaus, 2014; Katlein et al., 2019). Also at MOSAiC, in the first CO in October, snow depth and ice thickness had a positive correlation with R^2 up to 66% in the level part of the Sloop (**Figures 9** and **11**). This correlation is a result of preferential accumulation of snow on the rough and older non-ponded ice surfaces. While melt pond depressions can accumulate snow after snow redistribution events (Perovich et al., 2003; Anhaus et al., 2021; Webster et al., 2022) such situations may be transient and snow can be removed from them again in subsequent storms (Figure S1b and c).

In a calm period in December, in the absence of drifting snow events, thinly snow-covered surfaces grew faster and the relationship became negative, but R^2 remained low until the February storm. After the late February storm, snow distributed into dunes (**Figure 10**) that likely sintered and increased in density and thermal conductivity after a warm spell (**Figure 9**). Consequently, R^2 steadily increased to 77% by the beginning of April. This very high fraction of explained variability shows that snow depth was a strong governing factor for thermodynamic ice growth at MOSAiC. In addition, it suggests that layer-specific snow properties, like density, hardness and grain type (Sturm et al., 2002a; Merkouriadi et al., 2017), were less important than snow depth in controlling the effective snow thermal conductivity (Sturm et al., 2002b). The importance of the snow depth was likely intensified by the generally thin snow cover at MOSAiC (**Figure 7**).

This MOSAiC transect dataset provides the first spatially distributed observational data that clearly shows the seasonal development of the thermodynamic relationship between snow and ice. Observing the spatial distribution of snow on different sea ice thicknesses is an acknowledged challenge in the sea ice modeling community (Blazey et al., 2013; Castro-Morales et al., 2014). A limitation of our transect data is, however, that the sea ice thickness was derived by subtracting snow depth from total thickness. These two co-located data are not entirely independent. The findings from this paper need confirmation from other observational data, for example, from surface topography measured by terrestrial laser scanning (Clemens-Sewall et al., 2022) and bottom topography from underwater multibeam sonar (Nicolaus et al., 2022) or from high resolution numerical modeling.

Another limitation of our analysis is that we used a 50-m running mean over snow depth and sea ice thickness values along the transect tracks. This distance is in the middle range of the snow and sea ice patterns found in spectral analysis (**Figure 10**). A seasonally changing running mean length would likely result in even higher correlations, but such a method is difficult to apply uniformly on lines with different orientations to the predominant wind direction.

4. Conclusions

This paper gives a comprehensive description and analysis of a complete seasonal transect dataset that covers a range of sea ice cover thicknesses and snow depths on spatial scales of 10 km in the Eurasian part of the Arctic Ocean. Detailed analysis of the data focuses on the winter period of MOSAiC. The highlights of our findings and conclusions are:

1. The MOSAiC transects had relatively thin snow depths (approximately 0.1 to 0.3 m) and thick sea ice (modal sea ice thickness in May was 1.7 m), but within the ranges of the previously observed values. Based on the thin snow, thicker sea ice was expected.
2. At the start of the winter most of the transects included both level and deformed ice. By the end of the winter, ice dynamics decreased the fraction of level ice substantially, and by June only 12% of ice surfaces in the main transect line were level.

3. Storms diversified ice and snow cover through deformation and re-distribution. In the MOSAiC transect data, we observed how the standard deviation of both sea ice and snow thicknesses increased following early winter deformation events. In January, February and March, strong winds removed snow from level ice and deposited it into ice rubble and ridges.
4. Sea ice roughness is important for enhanced snow accumulation. A transect over previously ponded SYI following a deformation event in November covered roughly similar fractions of level ice, ice rubble, and ridges; the volume of snow on these surfaces in April was 18%, 45% and 36%, respectively. Sea ice roughness explained up to 85% (R^2) of the observed snow depth variability over both the level and deformed ice.
5. Winter thermodynamic processes homogenize the ice cover. The heat fluxes through thin snow on the remaining level ice can boost ice growth, diminishing the sea ice thickness differences between SYI and FYI. Sea ice thickness modes (representing level sea ice thickness) between these age categories were already similar during winter. From January onward, a separation between SYI and FYI based on sea ice thickness and snow depth was no longer possible. In April, snow explained up to 77% (R^2) of sea ice thickness variability over level ice. In addition, sea ice thickness exhibited spatial patterns similar to snow dunes, which implies that snow depth governs ice growth over level ice.
6. Melt ponds perpetuate their sea ice thickness and snow accumulation spatial distribution patterns into the winter. Preferential deposition of snow was observed on rough non-ponded areas until December, and thinner ice was detected in the areas previously occupied by melt ponds until January.

Apart from the old consolidated and newly formed ridges on the transects described in this paper, several dedicated ridge transects were accomplished at MOSAiC. The analysis of these transects will be the subject of separate papers.

This data description and basic analysis presented here does not exploit the full potential of the MOSAiC transect data. These data have already been used for calibration of remote sensing instruments (Munoz-Martin et al., 2020; Stroeve et al., 2020; Wagner et al., 2021) and model assessment (Webster et al., 2022). They are also crucial for upscaling studies of sea ice thickness and snow depth. The spatially distributed values collected by transects at the MOSAiC COs can be assessed for differences with regional point measurements, such as those collected by autonomous instrument (as in, e.g., Koo et al., 2021; Lei et al., 2022), and airborne regional total thickness measurements (von Albedyll et al., 2022). Both local and regional snow depth and sea ice thickness will be integral in the interdisciplinary framework of MOSAiC, and a critical resource of in situ data for numerical modeling work of various spatial resolutions as part of and beyond MOSAiC.

Data accessibility statement

All of the transect data used in this study are available in PANGAEA (Itkin et al., 2021; Hendricks et al., 2022). The Panomax images are available at Nicolaus et al. (2021). The MOSAiC meteorological data from RV *Polarstern* are available at Schmithüsen et al. (2021a), Schmithüsen et al. (2021c) and Schmithüsen et al. (2021b), while the precipitation data was provided by Matrosov et al. (2022). The data from climatology (Warren et al., 1999) were recreated by Ricker et al. (2014). The SHEBA data were downloaded from Sturm et al. (2007). The N-ICE data were downloaded from Rösel et al. (2016a) and Rösel et al. (2016b). Radarsat-2 data used in this paper were provided by NSA/KSAT through Canadian-Norwegian Radarsat-2 agreement. ALS data were provided by Stefan Hendricks and Arttu Jutila, AWI. The drone photo mosaics were provided by Steffen Graupner.

Supplemental files

The supplemental files for this article can be found as follows:

Supplemental Material.docx

Acknowledgments

This work was carried out and data used in this paper were produced as part of the international Multidisciplinary drifting Observatory for the Study of the Arctic Climate (MOSAiC) with the tag MOSAiC20192020. We thank all persons involved in the expedition of the RV *Polarstern* (Knust, 2017) during MOSAiC in 2019–2020 (AWI_PS122_00) as listed in Nixdorf et al. (2021). We are deeply grateful for the assistance in data collection from: Zoe Brasseur, Ulrike Dietrich, Alberto Enriquez, Allison Fong, Celia Gelfman, Marlene Goering, Jari Haapala, Antonia Immerz, Harold Jager, Tuija Jokinen, Arttu Jutila, Christian Katlein, Nikolai Kolabutin, Daniela Krampe, Benjamin Lange, Felix Linhardt, Amy Macfarlane, Marcel Nicolaus, Julia Regnery, Evgenii Salganik, Katrin Schmidt, Egor Shimanchuk, Katyanne Shoemaker, Matthew Shupe, Madison Smith, Gunnar Spreen, Aikaterini Tavri, Linda Thielke, Julienne Stroeve, Juarez Viegas, and the crew of the RV *Polarstern*. We also thank all the bear guards from all the science and logistic teams! We thank Malin Johansson (UiT) for assistance with the Radarsat-2 satellite data ordering. This paper was greatly improved by comments and suggestions of Jody Deming, Ruibo Lei and two anonymous reviewers.

Funding

This study has been partly funded by the international Multidisciplinary drifting Observatory for the Study of the Arctic Climate (MOSAiC) project with the tag MOSAiC 20192020 and the Project_ID: AWI_PS122_00. PI and GEL were funded by National Science Fundation (NSF) grant #1820927 (MiSNOW). PI was also supported by Research Council of Norway grant #287871 (SIDRiFT). SH, LvA, JR were funded by the AWI through the project AWI_ICE. MW acknowledges support by the National Aeronautics and Space Administration's New Investigator Program in Earth Science (#80NSSC20K0658). SA was supported by the German Research Council (DFG) in the

framework of the priority program "Antarctic Research with comparative investigations in the Arctic ice areas" (#SPP1158 and #AR1236/1). DD, MJ and MS were funded through EU-ARICE project DEARice. DD also acknowledges support of Research Council of Norway grant #280292 (HAVOC). MO was funded by NSF grant #OPP-1735862. IR was supported by NSF grant #OPP-1724540.

Competing interests

The authors have no competing interests, as defined by Elementa, that might be perceived to influence the research presented in this manuscript.

Author contributions

Contributed to conception and design: PI, SH, MW.

Contributed to field work planning and acquisition of data: SH, GEL, MS, MO, PI, MJ, DD, IR, RR, SA, MW, LA, JR.

Contributed to analysis and interpretation of data: PI, MW, SH, DD, MS, GEL.

Drafted and/or revised the article: PI, MW, SH, DD, LA, SA, RR, IR, JR, MJ, MO, GEL.

Approved the submitted version for publication: All authors.

References

Anhaus, P, **Katlein, C**, **Nicolaus, M**, **Hoppmann, M**, **Haas, C**. 2021. From bright windows to dark spots: Snow cover controls melt pond optical properties during refreezing. *Geophysical Research Letters* **48**(23): e2021GL095369. DOI: http://dx.doi.org/10.1029/2021GL095369.

Arndt, S, **Nicolaus, M.** 2014. Seasonal cycle and long-term trend of solar energy fluxes through Arctic sea ice. *The Cryosphere* **8**(6): 2219–2233. DOI: http://dx.doi.org/10.5194/tc-8-2219-2014.

Beckers, JF, **Renner, AH**, **Spreen, G**, **Gerland, S**, **Haas, C**. 2015. Sea-ice surface roughness estimates from airborne laser scanner and laser altimeter observations in Fram Strait and north of Svalbard. *Annals of Glaciology* **56**(69): 235–244. DOI: http://dx.doi.org/10.3189/2015AoG69A717.

Blazey, BA, **Holland, MM**, **Hunke, EC**. 2013. Arctic Ocean sea ice snow depth evaluation and bias sensitivity in CCSM. *The Cryosphere* **7**(6): 1887–1900. DOI: http://dx.doi.org/10.5194/tc-7-1887-2013.

Castellani, G, **Lüpkes, C**, **Hendricks, S**, **Gerdes, R.** 2014. Variability of Arctic sea-ice topography and its impact on the atmospheric surface drag. *Journal of Geophysical Research: Oceans* **119**(10): 6743–6762. DOI: http://dx.doi.org/10.1002/2013JC009712.

Castro-Morales, K, **Kauker, F**, **Losch, M**, **Hendricks, S**, **Riemann-Campe, K**, **Gerdes, R.** 2014. Sensitivity of simulated Arctic sea ice to realistic ice thickness distributions and snow parameterizations. *Journal of Geophysical Research: Oceans* **119**(1): 559–571. DOI: http://dx.doi.org/10.1002/2013JC009342.

Clemens-Sewall, D, **Polashenski, C**, **Raphael, I**, **Perovich, D**, **Fons, S**. 2022. High-resolution repeat topography of drifting ice floes in the Arctic Ocean from terrestrial laser scanning collected on the Multidisciplinary drifting Observatory for the Study of Arctic Climate expedition. Arctic Data Center. DOI: http://dx.doi.org/10.18739/A26688K9D.

Cohen, L, **Hudson, SR**, **Walden, VP**, **Graham, RM**, **Granskog, MA.** 2017. Meteorological conditions in a thinner Arctic sea ice regime from winter to summer during the Norwegian Young Sea Ice expedition (N-ICE2015). *Journal of Geophysical Research: Atmospheres* **122**(14): 7235–7259. DOI: http://dx.doi.org/10.1002/2016JD026034.

Cooley, JW, **Tukey, JW.** 1965. An algorithm for the machine calculation of complex Fourier series. *Mathematics of Computation* **19**(90): 297–301.

Eicken, H, **Tucker, WB**, **Perovich, DK**. 2001. Indirect measurements of the mass balance of summer Arctic sea ice with an electromagnetic induction technique. *Annals of Glaciology* **33**: 194–200. DOI: http://dx.doi.org/10.3189/172756401781818356.

Farrell, SL, **Duncan, K**, **Buckley, EM**, **Richter-Menge, J**, **Li, R**. 2020. Mapping sea ice surface topography in high fidelity with ICESat-2. *Geophysical Research Letters* **47**(21): e2020GL090708. DOI: http://dx.doi.org/10.1029/2020GL090708.

Forsström, S, **Gerland, S**, **Pedersen, CA**. 2011. Thickness and density of snow-covered sea ice and hydrostatic equilibrium assumption from in situ measurements in Fram Strait, the Barents Sea and the Svalbard coast. *Annals of Glaciology* **52**(57): 261–270. DOI: http://dx.doi.org/10.3189/172756411795931598.

Haas, C, **Beckers, J**, **King, J**, **Silis, A**, **Stroeve, J**, **Wilkinson, J**, **Notenboom, B**, **Schweiger, A**, **Hendricks, S.** 2017. Ice and snow thickness variability and change in the high Arctic Ocean observed by in situ measurements. *Geophysical Research Letters* **44**(20): 10462–10469. DOI: http://dx.doi.org/10.1002/2017GL075434.

Hansen, E, **Gerland, S**, **Granskog, MA**, **Pavlova, O**, **Renner, AHH**, **Haapala, J**, **Løyning, TB**, **Tschudi, M.** 2013. Thinning of Arctic sea ice observed in Fram Strait: 1990–2011. *Journal of Geophysical Research: Oceans* **118**(10): 5202–5221. DOI: http://dx.doi.org/10.1002/jgrc.20393.

Hendricks, S. 2009. Validierung von altimetrischen Meereisdickenmessungen mit einem helikopter-basierten elektromagnetischen Induktionsverfahren. Ph.D. thesis, University Bremen.

Hendricks, S, **Itkin, P**, **Ricker, R**, **Webster, M**, **von Albedyll, L**, **Rohde, J**, **Raphael, I**, **Jaggi, M**, **Arndt, S**. 2022. GEM-2 quicklook total thickness measurements from the 2019–2020 MOSAiC expedition. PANGAEA. DOI: http://dx.doi.org/10.1594/PANGAEA.943666.

Hunkeler, PA, **Hendricks, S**, **Hoppmann, M**, **Farquharson, CG**, **Kalscheuer, T**, **Grab, M**, **Kaufmann, MS**, **Rabenstein, L**, **Gerdes, R**. 2015a. Improved 1D inversions for sea ice thickness and conductivity from electromagnetic induction data: Inclusion of nonlinearities caused by passive bucking. *Geophysics* **81**(1): WA45–WA58. DOI: http://dx.doi.org/10.1190/geo2015-0130.1.

Hunkeler, PA, **Hendricks, S**, **Hoppmann, M**, **Paul, S**, **Gerdes, R**. 2015b. Towards an estimation of sub-sea-ice platelet-layer volume with multi-frequency electromagnetic induction sounding. *Annals of Glaciology* **56**(69): 137–146. DOI: http://dx.doi.org/10.3189/2015AoG69A705.

Iacozza, J, **Barber, DG**. 1999. An examination of the distribution of snow on sea-ice. *Atmosphere-Ocean* **37**: 21–51. DOI: http://dx.doi.org/10.1080/07055900.1999.9649620.

Itkin, P, **Spreen, G**, **Cheng, B**, **Doble, M**, **Girard-Ardhuin, F**, **Haapala, J**, **Hughes, N**, **Kaleschke, L**, **Nicolaus, M**, **Wilkinson, J**. 2017. Thin ice and storms: Sea ice deformation from buoy arrays deployed during N-ICE2015. *Journal of Geophysical Research: Oceans* **122**(6): 4661–4674. DOI: http://dx.doi.org/10.1002/2016JC012403.

Itkin, P, **Spreen, G**, **Hvidegaard, SM**, **Skourup, H**, **Wilkinson, J**, **Gerland, S**, **Granskog, MA**. 2018. Contribution of deformation to sea ice mass balance: A case study from an N-ICE2015 storm. *Geophysical Research Letters* **45**(2): 789–796. DOI: http://dx.doi.org/10.1002/2017GL076056.

Itkin, P, **Webster, M**, **Hendricks, S**, **Oggier, M**, **Jaggi, M**, **Ricker, R**, **Arndt, S**, **Divine, DV**, **von Albedyll, L**, **Raphael, I**, **Rohde, J**, **Liston, GE**. 2021. Magnaprobe snow and melt pond depth measurements from the 2019–2020 MOSAiC expedition. PANGAEA. DOI: http://dx.doi.org/10.1594/PANGAEA.937781.

Jutila, A, **Hendricks, S**, **Ricker, R**, **von Albedyll, L**, **Krumpen, T**, **Haas, C.** 2021. Retrieval and parametrisation of sea-ice bulk density from airborne multi-sensor measurements. *The Cryosphere Discussions* **2021**: 1–25. DOI: http://dx.doi.org/10.5194/tc-2021-149.

Katlein, C, **Arndt, S**, **Belter, HJ**, **Castellani, G**, **Nicolaus, M**. 2019. Seasonal evolution of light transmission distributions through Arctic sea ice. *Journal of Geophysical Research: Oceans* **124**(8): 5418–5435. DOI: http://dx.doi.org/10.1029/2018JC014833.

Katlein, C, **Mohrholz, V**, **Sheikin, I**, **Itkin, P**, **Divine, DV**, **Stroeve, J**, **Jutila, A**, **Krampe, D**, **Shimanchuk, E**, **Raphael, I**, **Rabe, B**, **Kuznetsov, I**, **Mallet, M**, **Liu, H**, **Hoppmann, M**, **Fang, YC**, **Dumitrascu, A**, **Arndt, S**, **Anhaus, P**, **Nicolaus, M**, **Matero, I**, **Oggier, M**, **Eicken, H**, **Haas, C**. 2020. Platelet ice under Arctic pack ice in winter. *Geophysical Research Letters* **47**(16): e2020GL088898. DOI: http://dx.doi.org/10.1029/2020GL088898.

King, J, **Skourup, H**, **Hvidegaard, SM**, **Rösel, A**, **Gerland, S**, **Spreen, G**, **Polashenski, C**, **Helm, V**, **Liston, GE**. 2018. Comparison of freeboard retrieval and ice thickness calculation from ALS, ASIRAS, and CryoSat-2 in the Norwegian Arctic to field measurements made during the N-ICE2015 expedition. *Journal of Geophysical Research: Oceans* **123**(2): 1123–1141. DOI: http://dx.doi.org/10.1002/2017JC013233.

Knust, R. 2017. Polar research and supply vessel POLARSTERN operated by the Alfred-Wegener-Institute. *Journal of Large-Scale Research Facilities* **3**. DOI: http://dx.doi.org/10.17815/jlsrf-3-163.

Koo, Y, **Lei, R**, **Cheng, Y**, **Cheng, B**, **Xie, H**, **Hoppmann, M**, **Kurtz, NT**, **Ackley, SF**, **Mestas-Nuñez, AM**. 2021. Estimation of thermodynamic and dynamic contributions to sea ice growth in the Central Arctic using ICESat-2 and MOSAiC SIMBA buoy data. *Remote Sensing of Environment* **267**: 112730. DOI: http://dx.doi.org/10.1016/j.rse.2021.112730.

Kwok, R. 2018. Arctic sea ice thickness, volume, and multiyear ice coverage: Losses and coupled variability (1958–2018). *Environmental Research Letters* **13**(10): 105005. DOI: http://dx.doi.org/10.1088/1748-9326/aae3ec.

Kwok, R, **Cunningham, GF**. 2016. Contributions of growth and deformation to monthly variability in sea ice thickness north of the coasts of Greenland and the Canadian Arctic Archipelago. *Geophysical Research Letters* **43**(15): 8097–8105. DOI: http://dx.doi.org/10.1002/2016GL069333.

Lee, SH, **McRoy, CP**, **Joo, HM**, **Gradinger, R**, **Cui, X**, **Yun, MS**, **Chung, KH**, **Kang, SH**, **Kang, CK**, **Choy, EJ**, **Son, S**, **Carmack, E**, **Whitledge, TE**. 2011. Holes in progressively thinning Arctic sea ice lead to new ice algae habitat. *Oceanography* **24**: 302–308. DOI: https://doi.org/10.5670/oceanog.2011.81.

Lei, R, **Cheng, B**, **Hoppmann, M**, **Zhang, F**, **Zuo, G**, **Hutchings, JK**, **Lin, L**, **Lan, M**, **Wang, H**, **Regnery, J**, **Krumpen, T**, **Haapala, J**, **Rabe, B**, **Perovich, DK**, **Nicolaus, M.** 2022. Seasonality and timing of sea ice mass balance and heat fluxes in the Arctic transpolar drift during 2019–2020. *Elementa: Science of the Anthropocene* **10**(1): 000089. DOI: http://dx.doi.org/10.1525/elementa.2021.000089.

Li, L, **Pomeroy, JW**. 1997. Estimates of threshold wind speeds for snow transport using meteorological data. *Journal of Applied Meteorology* **36**: 205–213. Available at https://www.jstor.org/stable/26182215.

Light, B, **Grenfell, TC**, **Perovich, DK**. 2008. Transmission and absorption of solar radiation by Arctic sea ice during the melt season. *Journal of Geophysical Research: Oceans* **113**(C3). DOI: http://dx.doi.org/10.1029/2006JC003977.

Lindsay, R, **Schweiger, A.** 2015. Arctic sea ice thickness loss determined using subsurface, aircraft, and satellite observations. *The Cryosphere* **9**(1): 269–283. DOI: http://dx.doi.org/10.5194/tc-9-269-2015.

Liston, GE, **Polashenski, C**, **Rösel, A**, **Itkin, P**, **King, J**, **Merkouriadi, I**, **Haapala, J**. 2018. A distributed snow-evolution model for sea-ice applications (SnowModel). *Journal of Geophysical Research: Oceans* **123**(5): 3786–3810. DOI: http://dx.doi.org/10.1002/2017JC013706.

Matrosov, SY, **Shupe, MD**, **Uttal, T.** 2022. High temporal resolution estimates of Arctic snowfall rates emphasizing gauge and radar-based retrievals from the MOSAiC expedition. *Elementa: Science of the*

Anthropocene **10**(1): 00101. DOI: http://dx.doi.org/10.1525/elementa.2021.00101.

Maykut, GA. 1978. Energy exchange over young sea ice in the central Arctic. *Journal of Geophysical Research* **83**: 3646–3658.

Merkouriadi, I, **Gallet, JC**, **Graham, RM**, **Liston, GE**, **Polashenski, C**, **Rösel, A**, **Gerland, S**. 2017. Winter snow conditions on Arctic sea ice north of Svalbard during the Norwegian young sea ICE (N-ICE2015) expedition. *Journal of Geophysical Research: Atmospheres* **122**(20): 10837–10854. DOI: http://dx.doi.org/10.1002/2017JD026753.

Munoz-Martin, JF, **Perez, A**, **Camps, A**, **Ribó, S**, **Cardellach, E**, **Stroeve, J**, **Nandan, V**, **Itkin, P**, **Tonboe, R**, **Hendricks, S**, **Huntemann, M**, **Spreen, G**, **Pastena, M.** 2020. Snow and ice thickness retrievals using GNSS-R: Preliminary results of the MOSAiC experiment. *Remote Sensing* **12**(24): 4038. DOI: http://dx.doi.org/10.3390/rs12244038.

Nicolaus, M, **Arndt, S**, **Birnbaum, G**, **Katlein, C**. 2021. Visual panoramic photographs of the surface conditions during the MOSAiC campaign 2019/20. PANGAEA. DOI: http://dx.doi.org/10.1594/PANGAEA.938534.

Nicolaus, M, **Perovich, DK**, **Spreen, G**, **Granskog, MA**, **von Albedyll, L**, **Angelopoulos, M**, **Anhaus, P**, **Arndt, S**, **Belter, HJ**, **Bessonov, V**, **Birnbaum, G**, **Brauchle, J**, **Calmer, R**, **Cardellach, E**, **Cheng, B**, **Clemens-Sewall, D**, **Dadic, R**, **Damm, E**, **de Boer, G**, **Demir, O**, **Dethloff, K**, **Divine, DV**, **Fong, AA**, **Fons, S**, **Frey, MM**, **Fuchs, N**, **Gabarró, C**, **Gerland, S**, **Goessling, HF**, **Gradinger, R**, **Haapala, J**, **Haas, C**, **Hamilton, J**, **Hannula, HR**, **Hendricks, S**, **Herber, A**, **Heuzé, C**, **Hoppmann, M**, **Høyland, KV**, **Huntemann, M**, **Hutchings, JK**, **Hwang, B**, **Itkin, P**, **Jacobi, HW**, **Jaggi, M**, **Jutila, A**, **Kaleschke, L**, **Katlein, C**, **Kolabutin, N**, **Krampe, D**, **Kristensen, SS**, **Krumpen, T**, **Kurtz, N**, **Lampert, A**, **Lange, BA**, **Lei, R**, **Light, B**, **Linhardt, F**, **Liston, GE**, **Loose, B**, **Macfarlane, AR**, **Mahmud, M**, **Matero, IO**, **Maus, S**, **Morgenstern, A**, **Naderpour, R**, **Nandan, V**, **Niubom, A**, **Oggier, M**, **Oppelt, N**, **Pätzold, F**, **Perron, C**, **Petrovsky, T**, **Pirazzini, R**, **Polashenski, C**, **Rabe, B**, **Raphael, IA**, **Regnery, J**, **Rex, M**, **Ricker, R**, **Riemann-Campe, K**, **Rinke, A**, **Rohde, J**, **Salganik, E**, **Scharien, RK**, **Schiller, M**, **Schneebeli, M**, **Semmling, M**, **Shimanchuk, E**, **Shupe, MD**, **Smith, MM**, **Smolyanitsky, V**, **Sokolov, V**, **Stanton, T**, **Stroeve, J**, **Thielke, L**, **Timofeeva, A**, **Tonboe, RT**, **Tavri, A**, **Tsamados, M**, **Wagner, DN**, **Watkins, D**, **Webster, M**, **Wendisch, M**. 2022. Overview of the MOSAiC expedition: Snow and sea ice. *Elementa: Science of the Anthropocene* **10**(1): 000046. DOI: http://dx.doi.org/10.1525/elementa.2021.000046.

Nixdorf, U, **Dethloff, K**, **Rex, M**, **Shupe, M**, **Sommerfeld, A**, **Perovich, DK**, **Nicolaus, M**, **Heuzé, C**, **Rabe, B**, **Loose, B**, **Damm, E**, **Gradinger, R**, **Fong, A**, **Maslowski, W**, **Rinke, A**, **Kwok, R**, **Spreen, G**, **Wendisch, M**, **Herber, A**, **Hirsekorn, M**, **Mohaupt, V**, **Frickenhaus, S**, **Immerz, A**, **Weiss-Tuider, K**, **König, B**, **Mengedoht, D**, **Regnery, J**, **Gerchow, P**, **Ransby, D**, **Krumpen, T**, **Morgenstern, A**, **Haas, C**, **Kanzow, T**, **Rack, FR**, **Saitzev, V**, **Sokolov, V**, **Makarov, A**, **Schwarze, S**, **Wunderlich, T**, **Wurr, K**, **Boetius, A.** 2021. MOSAiC extended acknowledgement. Zenodo. DOI: http://dx.doi.org/10.5281/zenodo.5541624.

Notz, D. 2009. The future of ice sheets and sea ice: Between reversible retreat and unstoppable loss. *Proceedings of the National Academy of Sciences* **106**(49): 20590–20595. DOI: http://dx.doi.org/10.1073/pnas.0902356106.

Onarheim, IH, **Eldevik, T**, **Smedsrud, LH**, **Stroeve, JC**. 2018. Seasonal and regional manifestation of Arctic sea ice loss. *Journal of Climate* **31**(12): 4917–4932. DOI: http://dx.doi.org/10.1175/JCLI-D-17-0427.1.

Perovich, DK, **Grenfell, TC**, **Richter-Menge, JA**, **Light, B**, **Tucker, WB III**, **Eicken, H**. 2003. Thin and thinner: Sea ice mass balance measurements during SHEBA. *Journal of Geophysical Research: Oceans* **108**(C3). DOI: http://dx.doi.org/10.1029/2001JC001079.

Perovich, DK, **Richter-Menge, JA**, **Jones, KF**, **Light, B**, **Elder, BC**, **Polashenski, C**, **Laroche, D**, **Markus, T**, **Lindsay, R**. 2011. Arctic sea-ice melt in 2008 and the role of solar heating. *Annals of Glaciology* **52**(57): 355–359. DOI: http://dx.doi.org/10.3189/172756411795931714.

Persson, POG, **Shupe, MD**, **Perovich, D**, **Solomon, A**. 2017. Linking atmospheric synoptic transport, cloud phase, surface energy fluxes, and sea-ice growth: Observations of midwinter SHEBA conditions. *Climate Dynamics* **49**: 1341–1364. DOI: http://dx.doi.org/10.1007/s00382-016-3383-1.

Pfaffling, A, **Haas, C**, **Reid, JE**. 2007. Direct helicopter EM—Sea-ice thickness inversion assessed with synthetic and field data. *GEOPHYSICS* **72**(4): F127–F137. DOI: http://dx.doi.org/10.1190/1.2732551.

Polashenski, C, **Perovich, D**, **Courville, Z**. 2012. The mechanisms of sea ice melt pond formation and evolution. *Journal of Geophysical Research: Oceans* **117**(C1). DOI: http://dx.doi.org/10.1029/2011JC007231.

Provost, C, **Sennéchael, N**, **Miguet, J**, **Itkin, P**, **Rösel, A**, **Koenig, Z**, **Villacieros-Robineau, N**, **Granskog, MA**. 2017. Observations of flooding and snow-ice formation in a thinner Arctic sea-ice regime during the N-ICE2015 campaign: Influence of basal ice melt and storms. *Journal of Geophysical Research: Oceans* **122**(9): 7115–7134. DOI: http://dx.doi.org/10.1002/2016JC012011.

Radionov, V, **Bryazgin, N**, **Alexandrov, E.** 1997. The snow cover of the Arctic basin. Applied Physics Laboratory, University of Washington. Originally published in Russian in Saint Petersburg by Gidrometeoizdat. English translation by Irina Solovyova and T. C. Grenfell.

Rampal, P, **Weiss, J**, **Marsan, D**. 2009. Positive trend in the mean speed and deformation rate of Arctic sea ice, 1979–2007. *Journal of Geophysical Research:*

Oceans **114**(C5). DOI: http://dx.doi.org/10.1029/2008JC005066.

Reid, JE, **Vrbancich, J**. 2004. A comparison of the inductive-limit footprints of airborne electromagnetic configurations. *Geophysics* **69**: 1229–1239.

Ricker, R, **Hendricks, S**, **Helm, V**, **Skourup, H**, **Davidson, M**. 2014. Sensitivity of CryoSat-2 Arctic sea-ice freeboard and thickness on radar-waveform interpretation. *The Cryosphere* **8**(4): 1607–1622. DOI: http://dx.doi.org/10.5194/tc-8-1607-2014.

Rösel, A, **Divine, D**, **King, JA**, **Nicolaus, M**, **Spreen, G**, **Itkin, P**, **Polashenski, CM**, **Liston, GE**, **Ervik, Å**, **Espeseth, M**, **Gierisch, A**, **Haapala, J**, **Maaß, N**, **Oikkonen, A**, **Orsi, A**, **Shestov, A**, **Wang, C**, **Gerland, S**, **Granskog, MA**. 2016a. *N-ICE2015 total (snow and ice) thickness data from EM31*. Tromsø, Norway: Norwegian Polar Institute. DOI: http://dx.doi.org/10.21334/npolar.2016.70352512.

Rösel, A, **Itkin, P**, **King, J**, **Divine, D**, **Wang, C**, **Granskog, MA**, **Krumpen, T**, **Gerland, S**. 2018. Thin sea ice, thick snow, and widespread negative freeboard observed during N-ICE2015 north of Svalbard. *Journal of Geophysical Research: Oceans* **123**(2): 1156–1176. DOI: http://dx.doi.org/10.1002/2017JC012865.

Rösel, A, **Polashenski, CM**, **Liston, GE**, **King, JA**, **Nicolaus, M**, **Gallet, JC**, **Divine, D**, **Itkin, P**, **Spreen, G**, **Ervik, Å**, **Espeseth, M**, **Gierisch, A**, **Haapala, J**, **Maaß, N**, **Oikkonen, A**, **Orsi, A**, **Shestov, A**, **Wang, C**, **Gerland, S**, **Granskog, MA**. 2016b. *N-ICE2015 snow depth data with Magnaprobe*. Tromsø, Norway: Norwegian Polar Institute. DOI: http://dx.doi.org/10.21334/npolar.2016.3d72756d.

Schmithüsen, H, **Raeke, A**, **Kieser, J**. 2021a. *Meteorological observations during POLARSTERN cruise PS122/1*. Bremerhaven: Alfred Wegener Institute, Helmholtz Centre for Polar and Marine Research. PANGAEA. DOI: http://dx.doi.org/10.1594/PANGAEA.935263.

Schmithüsen, H, **Rohleder, C**, **Hausen, R**. 2021b. *Meteorological observations during POLARSTERN cruise PS122/3*. Bremerhaven: Alfred Wegener Institute, Helmholtz Centre for Polar and Marine Research. PANGAEA. DOI: http://dx.doi.org/10.1594/PANGAEA.935265.

Schmithüsen, H, **Schröter, S**, **Wenzel, J.** 2021c. *Meteorological observations during POLARSTERN cruise PS122/2*. Bremerhaven: Alfred Wegener Institute, Helmholtz Centre for Polar and Marine Research. PANGAEA. DOI: http://dx.doi.org/10.1594/PANGAEA.935264.

Shupe, MD, **Rex, M**, **Dethloff, K**, **Damm, E**, **Fong, AA**, **Gradinger, R**, **Heuzé, C**, **Loose, B**, **Makarov, A**, **Maslowski, W**, **Nicolaus, M**, **Perovich, D**, **Rabe, B**, **Rinke, A**, **Sokolov, V**, **Sommerfeld, A**. 2020. Arctic Report Card 2020: The MOSAiC expedition: A year drifting with the Arctic sea ice. DOI: http://dx.doi.org/10.25923/9g3v-xh92.

Spreen, G, **Kwok, R**, **Menemenlis, D**. 2011. Trends in Arctic sea ice drift and role of wind forcing: 1992–2009. *Geophysical Research Letters* **38**(19). DOI: http://dx.doi.org/10.1029/2011GL048970.

Stroeve, J, **Nandan, V**, **Willatt, R**, **Tonboe, R**, **Hendricks, S**, **Ricker, R**, **Mead, J**, **Mallett, R**, **Huntemann, M**, **Itkin, P**, **Schneebeli, M**, **Krampe, D**, **Spreen, G**, **Wilkinson, J**, **Matero, I**, **Hoppmann, M**, **Tsamados, M**. 2020. Surface-based Ku- and Ka-band polarimetric radar for sea ice studies. *The Cryosphere* **14**(12): 4405–4426. DOI: http://dx.doi.org/10.5194/tc-14-4405-2020.

Stroeve, J, **Notz, D**. 2018. Changing state of Arctic sea ice across all seasons. *Environmental Research Letters* **13**(10): 103001. DOI: http://dx.doi.org/10.1088/1748-9326/aade56.

Sturm, M, **Holmgren, J**, **Perovich, D III, Tucker, T, Elder, B, Richter-Menge, J.** 2007. Snow cover measurements. Version 1.0. UCAR/NCAR - Earth Observing Laboratory, NCAR/EOL under the sponsorship of the National Science Foundation. DOI: http://dx.doi.org/10.5065/D6R20ZRW.

Sturm, M, **Holmgren, J**, **Perovich, DK**. 2002a. Winter snow cover on the sea ice of the Arctic Ocean at the Surface Heat Budget of the Arctic Ocean (SHEBA): Temporal evolution and spatial variability. *Journal of Geophysical Research: Oceans* **107**(C10): SHE 23–1–SHE 23–17. DOI: http://dx.doi.org/10.1029/2000JC000400.

Sturm, M, **Holmgren, J.** 2018. An automatic snow depth probe for field validation campaigns. *Water Resources Research* **54**(11): 9695–9701. DOI: http://dx.doi.org/10.1029/2018WR023559.

Sturm, M, **Massom, RA**. 2009. *Snow and sea ice*. New York, NY: John Wiley & Sons, Ltd: 153–204. DOI: http://dx.doi.org/10.1002/9781444317145.ch5.

Sturm, M, **Perovich, DK**, **Holmgren, J**. 2002b. Thermal conductivity and heat transfer through the snow on the ice of the Beaufort Sea. *Journal of Geophysical Research: Oceans* **107**(C10): SHE 19–1–SHE 19–17. DOI: http://dx.doi.org/10.1029/2000JC000409.

Torrence, C, **Compo, GP**. 1998. A practical guide to wavelet analysis. *Bulletin of the American Meteorological Society* **79**(1): 61–78. DOI: http://dx.doi.org/10.1175/1520-0477(1998)079<0061:APGTWA>2.0.CO;2.

Untersteiner, N. 1961. On the mass and heat budget of Arctic sea ice. *Archiv für Meteorologie, Geophysik und Bioklimatologie Serie A* **12**(2): 151–182.

Virtanen, P, **Gommers, R**, **Oliphant, TE**, **Haberland, M**, **Reddy, T**, **Cournapeau, D**, **Burovski, E**, **Peterson, P**, **Weckesser, W**, **Bright, J**, **van der Walt, SJ**, **Brett, M**, **Wilson, J**, **Millman, KJ**, **Mayorov, N**, **Nelson, ARJ**, **Jones, E**, **Kern, R**, **Larson, E**, **Carey, CJ**, **Polat, İ**, **Feng, Y**, **Moore, EW**, **VanderPlas, J**, **Laxalde, D**, **Perktold, J**, **Cimrman, R**, **Henriksen, I**, **Quintero, EA**, **Harris, CR**, **Archibald, AM**, **Ribeiro, AH**, **Pedregosa, F**, **van Mulbregt, P, SciPy 10 Contributors.** 2020. SciPy 1.0: Fundamental algorithms for scientific computing in Python. *Nature Methods* **17**: 261–272. DOI: http://dx.doi.org/10.1038/s41592-019-0686-2.

von Albedyll, L, **Hendricks, S**, **Grodofzig, R**, **Krumpen, T**, **Arndt, S**, **Belter, H**, **Cheng, B**, **Birnbaum, G**, **Hoppmann, M**, **Hutchings, J**, **Itkin, P**, **Lei, R**, **Nicolaus, M**, **Ricker, R**, **Rohde, J**, **Suhrhoff, M**, **Timofeeva, A**, **Watkins, D**, **Webster, M**, **Haas, C**. 2022. Thermodynamic and dynamic contributions to seasonal Arctic sea ice thickness distributions from airborne observations. *Elementa: Science of the Anthropocene* **10**(1): 00074. DOI: http://dx.doi.org/10.1525/elementa.2021.00074.

Wagner, DN, **Shupe, MD**, **Persson, OG**, **Uttal, T**, **Frey, MM**, **Kirchgaessner, A**, **Schneebeli, M**, **Jaggi, M**, **Macfarlane, AR**, **Itkin, P**, **Arndt, S**, **Hendricks, S**, **Krampe, D**, **Ricker, R**, **Regnery, J**, **Kolabutin, N**, **Shimanshuck, E**, **Oggier, M**, **Raphael, I**, **Lehning, M**. 2021. Snowfall and snow accumulation processes during the MOSAiC winter and spring season. *The Cryosphere Discussions* **2021**: 1–48. DOI: http://dx.doi.org/10.5194/tc-2021-126.

Warren, SG, **Rigor, IG**, **Untersteiner, N**, **Radionov, VF**, **Bryazgin, NN**, **Aleksandrov, YI**, **Colony, R**. 1999. Snow depth on Arctic sea ice. *Journal of Climate* **12**(6): 1814–1829. DOI: http://dx.doi.org/10.1175/1520-0442(1999)012<1814:SDOASI>2.0.CO;2.

Webster, M, **Gerland, S**, **Holland, M**, **Hunke, E**, **Kwok, R**, **Lecomte, O**, **Massom, R**, **Perovich, D**, **Sturm, M**. 2018. Snow in the changing sea-ice systems. *Nature Climate Change* **8**: 946–953. DOI: http://dx.doi.org/10.1038/s41558-018-0286-7.

Webster, MA, **Holland, M**, **Wright, NC**, **Hendricks, S**, **Hutter, N**, **Itkin, P**, **Light, B**, **Linhardt, F**, **Perovich, DK**, **Raphael, IA**, **Smith, MM**, **von Albedyll, L**, **Zhang, J**. 2022. Spatiotemporal evolution of melt ponds in the Arctic: MOSAiC observations and model result. *Elementa: Science of the Anthropocene* **10**(1): 000072. DOI: https://doi.org/10.1525/elementa.2021.000072.

Zygmuntowska, M, **Rampal, P**, **Ivanova, N**, **Smedsrud, LH**. 2014. Uncertainties in Arctic sea ice thickness and volume: New estimates and implications for trends. *The Cryosphere* **8**(2): 705–720. DOI: http://dx.doi.org/10.5194/tc-8-705-2014.

How to cite this article: Itkin, P, Hendricks, S, Webster, M, von Albedyll, L, Arndt, S, Divine, D, Jaggi, M, Oggier, M, Raphael, I, Ricker, R, Rohde, J, Schneebeli, M, Liston, GE. 2023. Sea ice and snow characteristics from year-long transects at the MOSAiC Central Observatory. *Elementa: Science of the Anthropocene* 11(1). DOI: https://doi.org/10.1525/elementa.2022.00048

Domain Editor-in-Chief: Jody W. Deming, University of Washington, Seattle, WA, USA

Associate Editor: Stephen F. Ackley, Department of Geological Sciences, University of Texas at San Antonio, TX, USA

Knowledge Domain: Ocean Science

Part of an Elementa Special Feature: The Multidisciplinary Drifting Observatory for the Study of Arctic Climate (MOSAiC)

Published: February 16, 2023 **Accepted:** December 07, 2022 **Submitted:** March 20, 2022

ELEMENTA Science of the Anthropocene

Elem Sci Anth is a peer-reviewed open access journal published by University of California Press.

OPEN ACCESS